ChemElectroChem

Research Article
doi.org/10.1002/celc.202400228

Chemistry Europe
European Chemical Societies Publishing

www.chemelectrochem.org

On the Stability of an Atomically-Dispersed Fe–N–C ORR Catalyst: An *In Situ* XAS Study in a PEMFC

Davide Menga[+],*[a] Yan-Sheng Li[+],*[a] Ana Marija Damjanović,[a] Olivier Proux,[b] Friedrich E. Wagner[†],[c] Tim-Patrick Fellinger,[d] Hubert A. Gasteiger,[a] and Michele Piana[a]

The stability of Fe–N–C oxygen reduction reaction (ORR) electrocatalysts has been considered a primary challenge for their practical application in proton exchange membrane fuel cells (PEMFCs). While several studies have attempted to reveal the possible degradation mechanism of Fe–N–C ORR catalysts, there are few research results reporting on their stability as well as the possible Fe species formed under different voltages in real PEMFC operation. In this work, we employ *in-situ* X-ray absorption near-edge structure (XANES) to monitor the active-site degradation byproducts of an atomically dispersed Fe–N–C ORR catalyst under a H_2/O_2-operating PEMFC at 90% relative humidity and 80 °C. For this, stability tests were carried out at two constant cell voltages, namely 0.4 and at 0.8 V. Even though the ORR activity of the Fe–N–C catalyst decreased significantly and was almost identical at the end of the tests for the two voltages employed, the analysis of the XANES recorded under H_2/N_2 configuration at 0.6 and 0.9 V within the stability test suggests that two different degradation mechanisms occur. They are demetalation of iron cations followed by their precipitation into Fe oxides upon operation at 0.8 V, versus a chemical carbon oxidation close to the active sites, likely triggered by reactive oxygen species (ROS) originated from the H_2O_2 formation, during the operation at 0.4 V.

Introduction

Proton exchange membrane fuel cells (PEMFCs) represent a crucial technology for clean-energy production and reduction of CO_2 emissions; nevertheless, their cost is one of the significant challenges for replacing the traditional combustion engines.[1] The core component of a PEMFC is the membrane electrode assembly (MEA), consisting of a polymer electrolyte membrane sandwiched between cathode and anode. In cathodes, a high loading of platinum group metal (PGM) catalysts, such as Pt, is typically required ($\geq 0.1\ mg_{Pt}cm^{-2}_{MEA}$) in order to catalyze the sluggish kinetics of the oxygen reduction reaction (ORR) and to deliver sufficient high-current density performance in PEMFCs.[2,3] According to a cost analysis on 80 kW PEMFC stacks, the ORR catalyst provides the major contribution to total costs upon further increasing their manufacturing volume.[4] Consequently, in order to reduce the cost of PEMFC stacks, finding alternative ORR catalysts that can reduce or replace PGMs has gained interest. In the family of PGM-free ORR catalysts, transition-metal- and nitrogen-co-doped carbon materials (M–N–C, where M=Fe, Co, or Mn) are the most studied alternatives. In particular, among all the M–N–C ORR catalysts, it was shown that Fe–N–C catalysts can achieve a beginning-of-test (BoT) ORR activity in PEMFCs comparable to those of Pt based ORR catalysts.[5–7]

Despite their promising initial performance in PEMFCs at BoT, Fe–N–C ORR catalysts suffer from poor stability and durability during PEMFC operations.[8] For a typical PEMFC based on Pt or Pt-alloy ORR catalysts, the life time can achieve hundreds of hours in an accelerated stress test (AST) with a reasonable performance at end-of-test (EoT).[9–11] However, this would be extremely challenging for PEMFCs based on Fe–N–C ORR catalysts, because their performance drops significantly in the initial few hours of durability and stability tests, far below the demands for automotive applications.[12,13] Studies have attributed the poor stability and durability of Fe–N–C ORR catalysts in PEMFCs to four possible degradation mechanisms, namely demetalation,[14,15] carbon oxidation (chemical and/or electrochemical),[16,17], micropore flooding,[18] and N-protonation followed by anion adsorption.[19] Among these four mechanisms, the first two are generally believed to be more probable, according to several theoretical and experimental findings. Regarding micropore flooding, where the term "micropore" relates to pores smaller than 2 nm, and N-protonation followed by anion adsorption, contradictory results have been reported,

[a] *D. Menga,[+] Y.-S. Li,[+] A. M. Damjanović, H. A. Gasteiger, M. Piana*
TUM School of Natural Sciences, Department of Chemistry and Catalysis Research Center, Chair of Technical Electrochemistry, Technical University of Munich, 85748 Garching, Germany
E-mail: menga@mit.edu
yan-sheng.li@tum.de

[b] *O. Proux*
Observatoire des Sciences de l'Univers de Grenoble (OSUG) UAR 832 CNRS, Univ. Grenoble Alpes, F-38041 Grenoble, France

[c] *F. E. Wagner*
TUM School of Natural Sciences, Department of Physics, Technical University of Munich, 85748 Garching, Germany

[d] *T.-P. Fellinger*
Bundesanstalt für Materialforschung und -Prüfung (BAM), 12203 Berlin, Germany

[+] *These authors contributed equally to the manuscript.*

[†] *Prof. Em. Friedrich E. Wagner passed away before this work was published.*

Supporting information for this article is available on the WWW under https://doi.org/10.1002/celc.202400228

therefore no consensus has been achieved for these two mechanisms.[20]

Demetalation of Fe from the active site has been widely reported in the literature[14–16,21] and different intermediates have been proposed to play a key role in its mechanism.[21,22] This process would consist of a loss of the coordination between nitrogen and atomic Fe in the Fe–N_4 active site, resulting in a decay of ORR activity. Many groups proposed that, after demetalation, the iron cations will ion-exchange into the perfluorosulfonic acid (PFSA) ionomer and/or possibly precipitate as iron oxide, depending on thermodynamics (deducible from the Pourbaix diagram) and kinetics at the specific conditions, like the concentration of iron cations, the pH, and the potential during operation.[6,23–26] On the other hand, carbon oxidation is believed to reduce the specific activity of the Fe–N_4 sites by introducing oxygen functionalities on their carbon neighbors, changing the electron density at the Fe active center.[17] Other studies also suggested that a strong oxidation may lead to the demetalation of Fe due to an extensive damage of the carbon support itself.[16,27,28] This oxidation can be either purely electrochemical (i.e., at a cathode potential higher than $\approx$1.3 V_{RHE})[16] or chemical (i.e., triggered by H_2O_2 and/or radicals attack).[17] The latter oxidation path is mainly attributed to the poor selectivity of Fe–N–C catalysts toward the ORR (i.e., to relatively slow reduction mechanisms of 2 electrons/O_2 and/or 2 + 2 electrons/O_2 instead of a fast direct 4 electrons/O_2 pathway), increasing the probability of Fenton-like reactions with further production of highly-reactive and detrimental radical species.[29] While all the above studies attempted to investigate the structural changes of the catalyst, there is no clear evidence on the potential dependency of one specific degradation mechanism.

The general understanding on structure–performance relationships of Fe–N–C catalysts has been pushed forward by spectroscopic techniques able to identify the active-site coordination environment at the atomic level. Mössbauer spectroscopy, for example, has proven fundamental in the development of Fe–N–C catalysts due to its ability to discern different Fe phases as well as different Fe coordinations.[23,30,31] On the other hand, the low amount of Fe present in this type of catalysts (usually $<$3 wt%) makes the data acquisition especially long. For this reason, X-ray absorption spectroscopy (XAS) employing synchrotron radiation has also been considered as a useful technique because of its high sensitivity and, consequently, its capability to probe samples with low amounts of Fe in the catalyst in a reasonable time. Therefore, XAS is often used *in situ* or *operando* to understand the working mechanism of Fe–N–C catalysts during operation.[24,32,33] Nevertheless, Mössbauer spectroscopy and XAS are bulk techniques which probe all Fe phases in the sample, therefore a Fe–N–C catalyst free from side phases is desirable in order to obtain meaningful data on the evolution of Fe active sites upon operation.[34] For this reason, one major challenge to understand the degradation mechanism of Fe–N–C ORR catalysts is to have a material containing mainly well-defined atomically-dispersed Fe–N_4 active sites. Typically, it is difficult to prepare Fe–N–C catalysts that are free from any Fe-containing side phases and with a high density of catalytically active sites. Lately, new synthetic approaches have proven to be able to synthesize only the desired active site free from side phases, pushing the understanding of these materials forward.[5,6,35–37]

In this study, we investigate the voltage dependence of the degradation of an atomically dispersed Fe–N–C ORR catalyst in an operating PEMFC using a 5 cm^2 membrane electrode assembly (MEA) under differential flow conditions. We first report the synthesis of an Fe–N–C catalyst on a Ketjenblack (KB) carbon support, employing an active-site imprinting method based on Zn^{2+} ions followed by low- and high-temperature Zn-to-Fe transmetalation. This method has proven to yield catalysts with well-defined tetrapyrrolic active sites free from other side phases like Fe carbide, Fe nitride, or metallic Fe.[36,38] Prior to the MEA fabrications, Mössbauer spectroscopic data elucidate the atomic structure of the as-synthesized catalyst powder, which mostly consists of atomically dispersed tetrapyrrolic Fe–N–C active sites ($\approx$90 wt% of total Fe content). To study the potential dependent degradation of the as-synthesized catalyst in a PEMFC, we employ constant-voltage stability tests at two operating cell voltages, namely 0.4 V and 0.8 V in the H_2/O_2 environment at 80 °C and 90% relative humidity (RH) over a total time of 3 hours. Fe oxidation state and formation of possible Fe side phases during the constant-voltage stability tests is monitored by *in situ* XAS (specifically focusing on X-ray Absorption Near-Edge Structure, XANES) at the beginning-of-test (BoT) and after 10, 30, 105 and 180 minutes (as end-of-test, EoT). The XAS spectra are collected under H_2/N_2 (anode/cathode) configuration at two cell voltages, namely 0.6 V (Fe^{2+}) and 0.9 V (Fe^{3+}), to control the oxidation state of the Fe species in the MEA. Based on the comparison of the XANES data collected during tests with standard Fe phases as references, we further discuss the evolution of Fe species upon degradation at two cell voltages, namely 0.4 V and 0.8 V.

Results and Discussion

Catalyst-Powder Characterization

To provide information about the Fe–N–C active-site structure and detect the presence of other possible Fe species in the catalyst powder, we first characterized it by Mössbauer spectroscopy.

Figure 1 shows the Mössbauer spectrum obtained at 4.2 K, consisting of two quadrupole doublets, usually identified as D1 (blue line, 75% in Table 1) and D2 (red line, 14% in Table 1), which are assigned to atomically dispersed Fe–N_4 sites. Based on literature reports and our previous work,[23,36,39,40] D1 is assigned to a Fe^{III}–N_4 site with an axial OH/O_2 ligand, while D2 is assigned to the square-planar Fe^{II}–N_4 moiety without OH/O_2 ligand. D1 is suggested to represent the real active sites, more active but less stable during the PEMFC operation, whereas D2 is attributed to the active sites which are more stable but less active.[23] In addition, the spectrum also exhibits a sextet component ($\approx$11% of the total Fe in the sample, see Table 1) attributed to nanoscopic Fe oxide. Due to their low amount

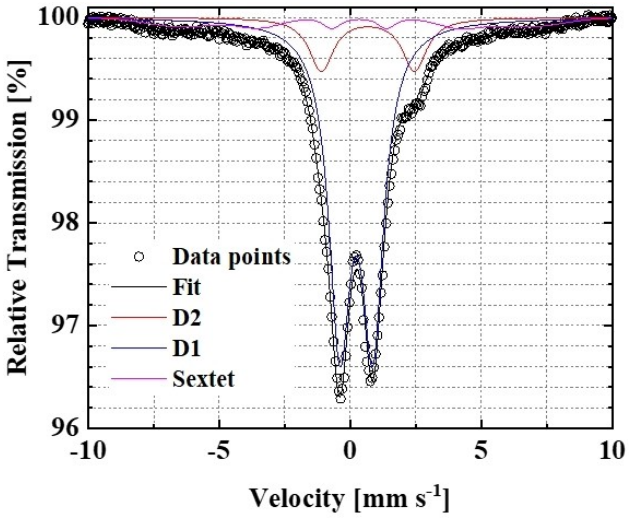

Figure 1. Mössbauer spectrum of the as-synthesized catalyst measured at 4.2 K.

compared to the Fe–N_4 sites, their presence is considered marginal for the XAS *in situ* analysis in the PEMFC. Upon cathode electrode preparation, the active-site structure might change due to coordination of OH/O_2 ligands to the Fe–N_4 sites, but no significant formation of iron oxide should take place.[41]

Stability of the Catalyst During the Performance Diagnostic

At the very beginning of this section, we briefly explain the rationale for designing the testing protocol used in this study (see Figure 11), specifically, we provide the reason why we only measured the LSV to determine the ORR activity at EoT. In general, it is common to check the PEMFC performance collecting a polarization curve or an LSV under O_2-fed cathode (either pure O_2 or air) and H_2-fed anode between aging procedures for a given testing protocol. This allows to track the ORR activity change of the catalyst over the course of the aging tests. Nevertheless, Fe–N–C ORR catalysts typically exhibit extremely poor stability during fuel-cell operation. Thus, prior to the investigation of the potential-dependent stability of the here investigated catalyst, we first evaluate its stability upon measuring consecutive LSVs to diagnose its ORR activity changes between each of them.

Figure 2a shows ten consecutively measured LSVs from OCV to 0.4 V cell voltage in H_2/O_2 configuration at 90% RH and 80 °C, using a slow scan rate of 2 mV s^{-1}. The cell voltages reported in Figure 2 are corrected by the HFR ($E_{HFR\text{-}free}$) determined at 0.6 V

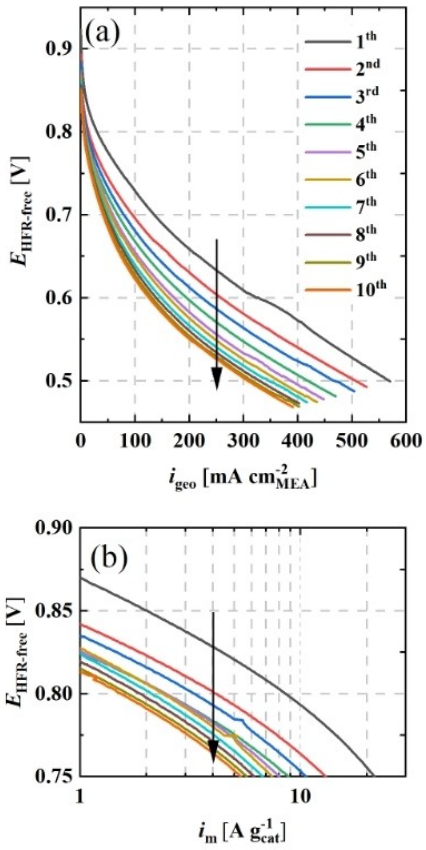

Figure 2. (a) HFR-corrected cell voltage ($E_{HFR\text{-}free}$) of ten consecutively measured LSVs (at 2 mV s^{-1}) obtained in H_2/O_2 configuration at 90% RH, 80 °C, and 150 $kPa_{abs,inlet}$ using the portable fuel cell test station for *in situ* XAS measurements. Each LSV is measured starting with OCV and scanning the cell voltage to 0.4 V. The HFRs are determined at 0.6 V after each LSV under the same conditions, and amount to 195 ± 5 mΩ cm^2_{MEA} upon averaging 10 measurements. (b) Tafel representations of the ten consecutively measured LSVs obtained from (a) using the mass-normalized current (i_m, A g^{-1}_{cat}). The loading of the cathode electrode is ≈3.5 mg_{cat} cm^{-2}_{MEA}. The black arrow indicates the trend from the 1st to 10th LSV, indicating that the MEA performance gradually drops from the 1st to the 10th LSV.

right after each LSV using the PEIS technique (see Experimental section). The HFRs of the ten LSVs average to 195 ± 5 mΩ cm^2_{MEA}, without any clear decreasing or increasing trend during the 10 consecutive measurements. From the results in Figure 2a it is evident that the H_2/O_2 performance of the MEA drops significantly while recording just LSVs. The geometric current density (i_{geo}) at $E_{HFR\text{-}free}$ = 0.6 V decreases by ≈60% after consecutively measuring 10 LSVs, namely from ≈340 mA cm^{-2}_{MEA} for the 1st LSV (in black) to ≈130 mA cm^{-2}_{MEA} for the 10th LSV (in orange).

Table 1. Isomer shift (IS), quadrupole splitting (QS), magnetic field (H) and relative abundance (%) of each species obtained from the fitting of the Mössbauer spectra of the catalyst powder at the temperature of 4.2 K.

Assigned peak	D1			D2			Sextet		
	IS	QS	%	IS	QS	%	IS	H	%
	0.23	1.26	75	0.67	3.56	14	0.26	40.8	11

To further extract the kinetic parameters regarding the cathode catalyst for each LSV, the Tafel representations are derived by normalizing the current shown in Figure 2a to the catalyst loading ($\approx$3.5 $mg_{cat}\,cm^{-2}_{MEA}$) to obtain the mass activity ($A\,g^{-1}_{cat}$). The mass-normalized current shown here is not corrected for the H_2-cross-over current and the ohmic shorting current of the membrane. This is because Fe–N–C ORR catalysts are not electrochemical active towards H_2 within the potential window of PEMFC operation and the MEAs fabricated here did not have ohmic shorting of the membrane. The initial ORR mass activity determined at $E_{HFR\text{-}free}$ = 0.8 V is $\approx$9.6 $A\,g^{-1}_{cat}$ (in black), whereas that of the 2nd LSV is $\approx$5 $A\,g^{-1}_{cat}$ (in red), corresponding to a mass activity loss of already $\approx$50% between the first and the second LSV, despite the very short time scale of collecting an LSV (only $\approx$5 min per LSV). This shows that it was not possible to check the LSV performance over the course of the constant-voltage stability tests, as even the short LSV already significantly affects the ORR activity. A similar experiment was previously conducted by Osmieri *et al.*, who also observed significant activity losses of an Fe–N–C ORR catalyst upon collection of polarization curves with O_2-fed cathodes.[13] The authors compared the voltage-cycling accelerated stress tests (VC-ASTs) using a N_2-fed cathode with and without measuring polarization curves between them, and found that the tests including polarization curves exhibited a much poorer ORR activity at the EoT. Therefore, it was concluded that the impact of the LSV performance test with an O_2-fed cathode leads to additional severe Fe–N–C catalyst degradation. While the mechanism of this degradation needs to be further studied and could be highly catalyst-dependent, it is crucial to avoid the LSV diagnostic under H_2/O_2 in our specific study, where we aimed to solely understand and evaluate the potential dependency of the Fe–N–C ORR catalyst degradation in a PEMFC.

Based on the results shown in Figure 2, aiming to avoid any degradation due to the LSVs under H_2/O_2, we conducted a specific protocol that only measures a LSV in H_2/O_2 (anode/cathode) at EoT to determine the EoT ORR activity of the catalyst. The details of the protocol are shown in Figure 11 in the Experimental section. In brief, the stability tests were conducted by using a constant-voltage protocol in H_2/O_2 configuration in two PEMFCs at different cell voltages of 0.4 and 0.8 V, for a total of 3 hours. For the sake of simplicity, we refer to the two protocols as "H_2/O_2 @ 0.4 V" and as "H_2/O_2 @ 0.8 V". The XAS spectra are collected in H_2/N_2 configuration within the stability tests to further elucidate the evolution of the oxidation state of Fe in the catalyst. It should be noted that the catalyst activity in the PEMFC was also tested by an LSV in H_2/O_2 after 20 consecutive XAS spectra in H_2/N_2 configuration had been acquired over a total time of $\approx$8.5 hours; the results (data not shown) indicate that the ORR activity is not affected by recording the XAS spectra of the cathode under H_2/N_2 configuration. Therefore, any change of the XAS spectra can be only attributed to the stability tests.

Geometrical Current Density during Constant-Voltage PEMFC Tests for *in situ* XAS

Figure 3a and b show the geometrical current density (i_{geo}, $mA\,cm^{-2}_{MEA}$) during the 3 hours of constant-voltage stability test in H_2/O_2 @ 0.4 V (a) and H_2/O_2 @ 0.8 V (b), respectively. Note that the results in Figure 3 are exactly the PEMFCs used to collect the XAS data reported later in this section.

Both profiles show a similar behavior, specifically, a fast decay of i_{geo} is observed in the first $\approx$30 minutes, followed by a much slower decay until EoT (after 180 minutes). To further compare results from the two testing protocols, the geometrical current densities at a given time ($i_{geo,t}$) were normalized to the initial current density ($i_{geo,t=0}$), and the results plotted in Figure 3c. It shows that a much stronger relative decay occurs upon testing in H_2/O_2@0.8 V (blue curve) compared to that in H_2/O_2@0.4 V (red curve). In the first $\approx$30 minutes, $\approx$80% of the current is already lost in the former case, while only $\approx$30% decay is observed in the latter case. After 3 hours (EoT), 90% of

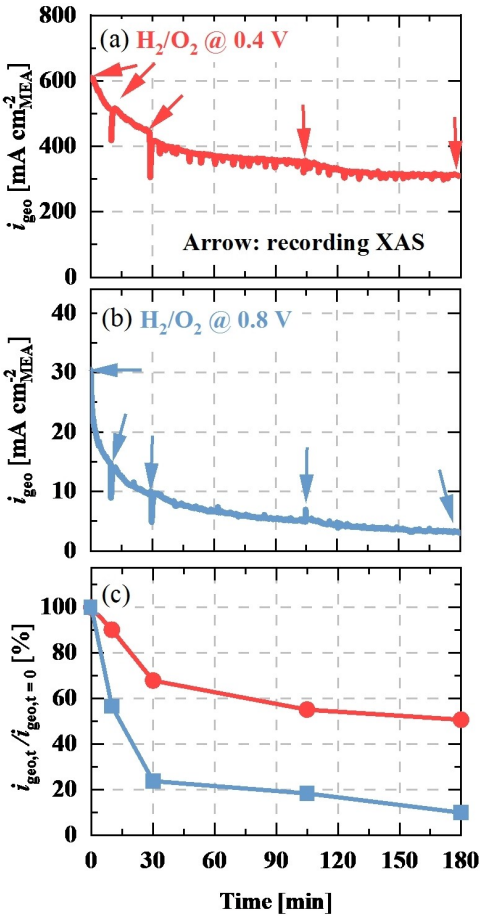

Figure 3. Geometrical current densities (i_{geo}, $mA\,cm^{-2}_{MEA}$) over 180 minutes of constant-voltage stability tests in H_2/O_2@0.4 V (a) and H_2/O_2@0.8 V (b), recorded in H_2/O_2 configuration (400 nccm for both anode and cathode) at 90% RH, 80 °C, and 150 $kPa_{abs,inlet}$. The arrows correspond to the times where XAS data were collected *in situ* in H_2/N_2 configuration (at both 0.6 and 0.9 V, spectra shown in Figures 7 and 9), i.e., at 0 (BoT), 10, 30, 105 and 180 minutes (EoT). (c) Relative decay of the geometrical current density normalized to its initial value at t = 0 minutes ($i_{geo,t}$ /$i_{geo,t=0}$ in %). The loading of cathode electrode for both MEAs is $\approx$3.5 $mg_{cat}\,cm^{-2}_{MEA}$.

the current is lost upon testing in H_2/O_2@0.8 V, whereas 50% of the current remains upon holding the cell voltage in H_2/O_2@0.4 V.

Compared to the literature, our results show similarities to other studies on the stability of Fe–N–C ORR catalysts upon constant-voltage tests in PEMFCs; in particular, the literature reports a fast current decay at initial stages of the test, followed by a subsequently much slower current decay. For example, Chenitz *et al.* reported an initial fast decay of the geometrical current density in the first ≈25 hours, followed by a slow decay (25–125 hours) using various constant cell voltages (from 0.2 V to 0.8 V) in a single PEMFC under H_2/air configuration.[14]. Similar observations were also reported by Zhang *et al.*, using a constant cell voltage of 0.6 V in both H_2/air and H_2/O_2 configurations.[42] Both publications attributed this unique current decay profile to the demetalation of Fe from the $Fe–N_4$ active site. In the latter publication, a numerical fitting of the resulting current decay profile was performed, suggesting that the initial fast decay is attributed to the Fe demetalation from active sites located in the micropores, whereas the slow decay is attributed to those located in the mesopores. Nevertheless, recently Yin *et al.* argued against the validity of this model based on two reasons: firstly, that it is incorrect to use the current decay obtained from the transport-controlled high-current density region (i.e., at low cell voltage, <0.7 V) to extract kinetic information of the catalyst; secondly, that the demetalation mechanism in micropores proposed by Zhang *et al.*, considering the Le Chatelier's principle, would be over-simplified, as the model neglects thermodynamic considerations such as the demetalation enthalpy or the bonding energy of $Fe–N_4$ sites.[43] According to another study from Yin *et al.*, the current decay obtained upon holding the cell voltage at 0.84 V fits well when considering a logistic (non-exponential) decay of an autocatalytic model, which can result from the degradation mechanism of $^{\bullet}OH$ radical attack to the catalyst due to the presence of H_2O_2.[44]

While the actual reason leading to this unique current density decay is still under debate, to further understand the possible causes of this loss in current density for the presented catalyst, we also tried to relate it to the presence of H_2O_2 by performing a rotating ring disk electrode (RRDE) experiment to quantify the H_2O_2 yield (H_2O_2%) of the catalyst (Figure A1). The results indicate that our catalyst exhibits a higher H_2O_2 yield at ≈0.4–0.55 V_{RHE} (≈6%), whereas it is negligible/non-detectable (close to 0%) at 0.8 V_{RHE}. Accordingly, the impact of H_2O_2 on the catalyst stability should be more significant in our case upon holding the cell voltage at 0.4 V in comparison to 0.8 V, apparently in contradiction with the observed much higher current density decay (up to 90% loss, see Figure 3c) upon holding the cell voltage at 0.8 V. Nevertheless, we would like to reiterate the statement from Yin *et al.* that when holding the cell voltage at relatively low voltage, as in our case at 0.4 V, the current density loss may not represent kinetic losses due to typically high mass transport losses in the high-current density region. Consequently, to compare the change in catalyst activity upon the given stability tests, we performed an LSV at the EoT for the two cases.

ORR Activity at EoT in PEMFCs Tests for in situ XAS

Figure 4a shows the Tafel representations of the LSV at EoT (with the current normalized to the cathode catalyst loading), measured immediately after the stability tests in H_2/O_2@0.8 V (in blue) and H_2/O_2@0.4 V (in red). For comparison, the LSV of a pristine MEA (i.e., not subjected to any preceding polarization curve or LSV) is also plotted (in black). The cell voltages in Figure 4a are corrected for the HFR ($E_{HFR\text{-}free}$) determined at 0.6 V right after each LSV, getting HFRs of 200 $m\Omega\,cm^{-2}_{MEA}$ and 191 $m\Omega\,cm^{-2}_{MEA}$ for H_2/O_2@0.8 V and H_2/O_2@0.4 V, respectively, which we consider essentially identical to the BoT HFR values (≈195 ± 5 $m\Omega\,cm^{-2}_{MEA}$).

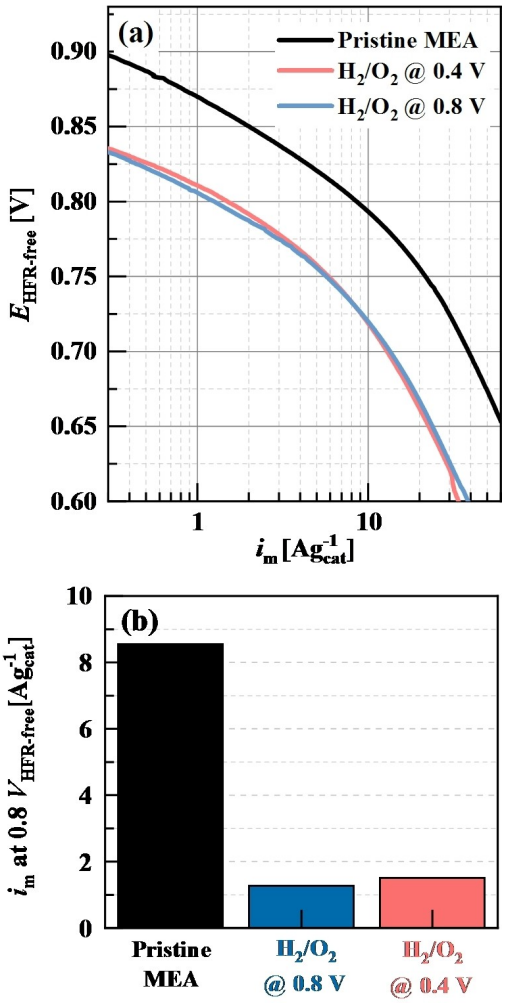

Figure 4. (a) Tafel representation derived from the LSVs (2 $mV\,s^{-1}$) using the flow fields for *in situ* XAS measurements and the portable test station in H_2/O_2 configuration (400 nccm for both anode and cathode) at 80 °C, 90% RH, and 150 $kPa_{abs,inlet}$: of the pristine MEA (i.e., without any previous aging or LSV measurement, in black), the MEA after a 3-hour constant voltage test at 0.8 V (in blue), and the MEA after a 3-hour constant voltage test at 0.4 V (in red). The currents (i_m, $A\,g^{-1}_{cat}$) are normalized to the loading of cathode electrode (≈3.5 $mg_{cat}\,cm^{-2}_{MEA}$ in all cases). The cell voltages ($E_{HFR\text{-}free}$) are corrected by the HFR determined at 0.6 V under the same conditions (200 and 191 $m\Omega\,cm^{-2}_{MEA}$ for the H_2/O_2@0.8 V and the H_2/O_2@0.4 V condition, respectively). (b) Mass activities (i_m) of the three MEAs calculated from Figure 4a by extracting the value of i_m at 0.8 $V_{HFR\text{-}free}$.

Similarly to what we observed for a different catalyst,[34] looking at Figure 4a, the EoT Tafel representations for the catalyst aged at both potentials surprisingly overlap and show a significant performance loss compared to the pristine MEA. A voltage loss of ≈70 mV is observed at the same current density up to ≈10 $A g^{-1}_{cat}$ (≡35 $mA cm^{-2}_{MEA}$). By considering simple Tafel kinetics, this voltage drop indicates an increased ORR overpotential for the aged MEAs. The determination of i_m at the reversible potential (i.e., the exchange current density) should ideally be done by applying a linear regression to the Tafel representation, covering at least a decade of current change. However, as the Tafel representations in Figure 4a exhibit two slopes for all the cases (pristine and aged MEAs), this may lead to a misinterpretation. Generally, it is believed that the two different Tafel slopes of the Fe–N–C catalyst originate from the potential-dependent oxidation state of the iron in Fe–N_4 sites. At high voltage (usually above 0.75 V), the Fe oxidation state is high (close or equal to Fe^{3+}), in which case adsorbed OH species are postulated to limit O_2 adsorption, thereby decreasing the ORR activity (leading to the low Tafel slope above 0.75 V). On the other hand, when the voltage is low (usually below 0.75 V), the Fe oxidation state is lower (close or equal to Fe^{2+}), in which case OH species are released, and the active sites becomes available to the adsorption of molecular oxygen. This typically results in the second, higher Tafel slope below 0.75 V). Nevertheless, it is noteworthy that substantial transport loss across the electrode might occur for the here used very thick cathodes (≈100 μm in our case), resulting in additional voltage losses.

For this reason, to precisely quantify the ORR activity decay after the stability tests, the mass activity is determined using i_m at 0.8 $V_{HFR\text{-}free}$ from Figure 4a, which is reported in Figure 4b. In agreement with the Tafel representations in Figure 4a, it is evident that the mass activities of aged MEAs after the constant-voltage stability tests at both potentials are almost identical (see blue and red bars in Figure 4b), showing a mass activity loss of ≈80% (to ≈1.3–1.5 $A g^{-1}_{cat}$) compared to the pristine MEA (≈8.3 $A g^{-1}_{cat}$, see black bar).

To ensure that the similar mass activities at EoT of both tests are not related to the special flow fields used for XAS data collection, we replicated these tests using standard 5 cm^2 flow fields (single channel/7-serpentines) tested on a Greenlight G60 fuel cell test station. A similar comparison, using a commercial PGM-free cathode catalyst from Pajarito Powder, was previously reported in a publication from our group, showing that both setups provide comparable MEA degradation and ORR activity.[34] Consistent with this, essentially identical results are obtained also here in the low-current density region (i.e., up to ≈10 $A g^{-1}_{cat}$ or 35 $mA cm^{-2}_{MEA}$), where mass transport resistances are negligible (see Figure A2); consequently, the EoT ORR mass activities at 0.8 $V_{HFR\text{-}free}$ of ≈1.1 $A g^{-1}_{cat}$ for both potential holds are very similar to those obtained with the *in situ* XAS flow field (Figure 4b).

The observation that the ORR activities of the catalysts are similar at EoT regardless of the potential during the aging test suggests similar degradation kinetics of the catalyst at both 0.4 and 0.8 V. It is also important to remark on the poor stability of the Fe–N–C catalyst synthesized for this study, which degraded severely within only 3 hours of the constant-voltage stability test. In fact, comparing our results to those reported by Zhang *et al.*, Chenitz *et al.*, and Yin et al, despite the similar current density decay (i.e., initially fast followed by a slower decay), our catalyst only exhibits ≈30 minutes fast initial current decay. In contrast, the catalysts tested in those publications took at least ≈10 hours or more.[14,42,44]

Cyclic Voltammetry (CV) at BoT and EoT

To provide additional information on the catalyst characteristics before and after the stability tests, Figure 5a and b present the cyclic voltammograms of the cathodes used in the H_2/O_2@0.8 V and H_2/O_2@0.4 V tests, respectively, recorded in H_2/N_2 configuration (anode/cathode) at BoT and EoT (note that the currents are normalized by the cathode catalyst loading [$A g^{-1}_{cat}$]).

Comparing the two CVs at BoT (solid lines in Figure 5a and b) demonstrates that the measurements are reproducible, with two redox features at ≈0.8 V (anodic scan) and ≈0.75 V (cathodic scan), typically attributed to the Fe^{3+}/Fe^{2+} redox of Fe–N–C catalysts.[32,33] After the stability tests, small differences are observed: at EoT of the H_2/O_2@0.8 V test, the Fe^{3+}/Fe^{2+} redox feature in the CV (blue dashed line in Figure 5a) slightly decreases; on the other hand, the CV after EoT of the H_2/O_2@0.4 V test (dashed red line in Figure 5b) shows a remarkable difference, namely a broad feature at ≈0.4–0.8 V overlaying on the Fe^{3+}/Fe^{2+} redox from BoT. Similar observations were reported by Banham *et al.* and Osmieri *et al.*[12,13], who sug-

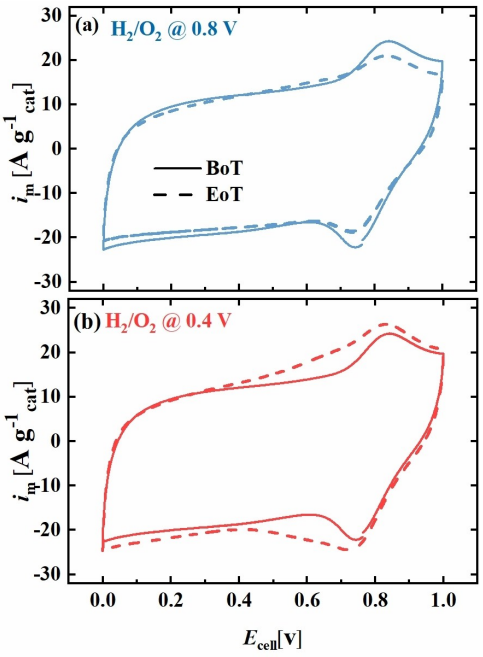

Figure 5. CV recorded at BoT (solid lines) and EoT (dashed lines) in H_2/N_2 configuration (400 nccm both anode and cathode) at 80 °C, 90% RH, and 150 $kPa_{abs/inlet}$: (a) MEA used for the H_2/O_2@0.8 V test (blue); (c) MEA used for the H_2/O_2@0.4 V test (red). The y-axis shows the mass-normalized current (i_m, $A g^{-1}_{cat}$) using the cathode catalyst loading of the MEAs (≈3.5 $mg_{cat} cm^{-2}_{MEA}$).

gested that this increase in pseudocapacitance corresponds to the quinone/hydroquinone redox, i.e., to the contribution from oxygen-containing functional groups on the carbon surface. Their presence was previously ascribed to the chemical oxidation of the carbon support due to the attack of reactive •OH or other oxygen-containing radicals.[45] It is hypothesized that these radicals are produced through a Fenton-like reaction due to the presence of H_2O_2 and Fe in the Fe–N–C cathode. This is indeed consistent with the much higher H_2O_2 yield at 0.4 V (see Figure A1), from which we conclude that the major degradation mechanism during the H_2/O_2@0.4 V test is likely related to the radical attack on the carbon support. According to Choi *et al.*, such degradation is not linked to the loss of Fe atoms from the Fe–N_4 sites, but to the formation of oxygen-containing functional groups near the Fe–N_4 sites, which weaken the binding energy between oxygen and the Fe active sites, thereby decreasing the ORR activity.[17] However, these still rather minor changes in the CVs are insufficient to provide a solid conclusion. Therefore, the investigation on the degradation mechanism of the Fe–N–C catalyst will be complemented by *in situ* XAS measurements, which are discussed in detail in the following sections.

In situ XAS during the Stability Tests in PEMFCs

Before discussing the XAS data collected during the stability tests in H_2/O_2, it is very important to understand the penetration depth of the incident X-ray beam, as well as the attenuation of the fluorescence beam. For the typically used high catalyst loadings for PGM-free catalyst-based cathodes, rather thick electrodes are obtained (≈100 μm in our case).[46] For this reason, if only a certain portion of the MEA is probed during the experiments, e.g., only the cathode or even only a part of it, and if this is not taken into account, misleading conclusions might be drawn.

To calculate X-ray attenuation/transmission at a given energy through different materials, online calculators are available, like that provided by the GeoSoilEnviro Center for Advanced Radiation Sources (GSECARS) at the University of Chicago.[47] For this calculation, the densities (ρ, g cm^{-3}) and effective thicknesses (t_{eff}, μm, taking into account the porosity) of each component in the MEA are needed, together with the beam energies (45° incident beam at the Fe K-edge of 7112 eV and 45° fluorescent beam at the $K_{\alpha 1}$ Fe emission line of 6405 eV). Based on the calculations (see Table A2), the 0.5 mm-thick graphite window is the component which most strongly attenuates the incident beam (fraction transmitted of the incident beam is ≈8.7%). In the MEA, the electrodes can be considered as ≈60% porous carbon, with marginal attenuation, while the PEM is approximated as a PTFE foil with a density of ≈2 g/cm^3, obtaining a transmitted beam fraction for the entire MEA (i.e., GDLs, catalyst layers, and PEM) of ≈38% (note that the attenuation caused by the PEM water uptake is negligible). This indicates that the signal measured in fluorescence is characteristic of the entire MEA.

Another important observation concerns the stability of the X-ray absorption raw intensity (before normalization) during the electrochemical stability test. From Figure A3 in the appendix, no strong variation is evident in the edge jump at EoT compared to BoT. This is strong evidence of the fact that most of Fe stays in the MEA and is not washed away with the produced water.

XANES Spectra of the Pristine MEA

Figure 6a shows the XANES spectra at the Fe K-edge of the pristine MEA (without any preceding LSV or stability test) recorded at different cell voltages under H_2/N_2 on anode/

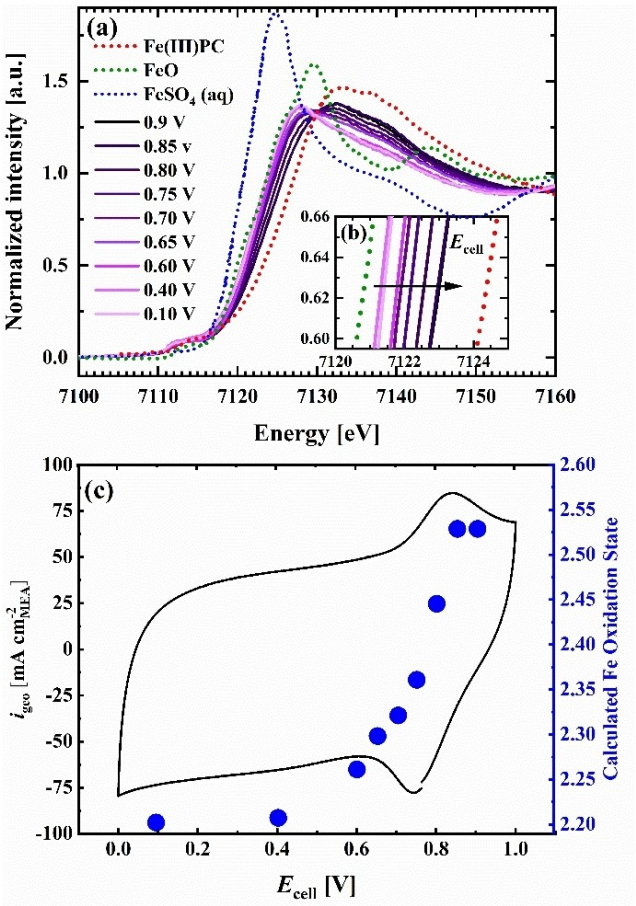

Figure 6. (a) XANES spectra at the Fe K-edge of the pristine MEA (cathode loading: ≈3.5 mg_{cat} cm^{-2}) measured at cell voltages of 0.1, 0.4, 0.6, 0.65, 0.7, 0.75, 0.8, and 0.9 V in H_2/N_2 (anode/cathode, both at 400 nccm) at 90% RH, 80 °C, and 150 $kPa_{abs,inlet}$. The darkest purple to the lightest purple solid lines indicate the XANES recorded from 0.9 V to 0.1 V. The spectra of Fe reference phases are Fe(III)-phthalocyanine (Fe(III)Pc, red-dashed line), FeO (green-dashed line), and $FeSO_4$ (aq) (blue-dashed line). The spectra of $FeSO_4$ (aq) at 0.5 M concentration were digitalized from reference,[24] while the data of Fe(III)Pc is obtained from reference.[32] (b) Detail of the shift in edge positions with cell voltage extracted from the spectra in (a). (c) Calculated Fe oxidation state of the pristine MEA (in blue, right *y*-axis) at each measured voltage based on a linear combination fitting (LCF) of each spectrum shown in (a), composed of the spectral response of the Fe(III)Pc and FeO as Fe^{3+} and Fe^{2+} reference samples, respectively. The details of this calculation are further described in the text. The CV (plotted in black) is obtained from the BoT sample (same as in Figure 5).

cathode (from 0.9 V to 0.1 V, from the darkest to the lightest purple line), acquired at 90% RH, 80 °C, and 150 $kPa_{abs,inlet}$. The XANES spectra of the pristine MEA show a strongly voltage-dependent iron oxidation state, i.e., upon increasing the cell voltage, the oxidation state of Fe is increased, as evident from the shift toward higher energy of the edge position (see Figure 6b). This observation is consistent with other studies reporting *in situ* XANES experiments on Fe–N–C catalysts in both RDE and fuel cell.[32,33] It has been suggested that the fraction of Fe(III) and Fe(II) in the Fe–N–C active sites is governed by the applied potential,[48] which typically has a redox transition at ≈0.6–0.8 V, depending on the atomic structure and the activity of the Fe–N–C catalysts.[33]

To provide a quantitative insight on the potential-dependent oxidation state of iron in the pristine MEA, we further calculated the average oxidation state at each measured cell voltage by using the approach given by Osmieri *et al.*[32] In brief, the XANES regions of the spectra (from 7104 eV to 7154 eV) are analyzed using a linear combination fitting (LCF) of two reference samples, namely FeO (green line in Figure 6a) and Fe(III)-phthalocyanine (Fe(III)Pc, red line in Figure 6a), representing Fe^{2+} and Fe^{3+}, respectively. This provides the atomic fractions of Fe at each oxidation state, which can be multiplied by the corresponding charges (i.e., Fe^{3+} and Fe^{2+}) and then summed to get the average oxidation state. Please note that according to Osmieri *et al.*, the FeO instead of Fe(II)Pc was selected as reference sample to avoid the strong peak of Fe(II)Pc at the edge, which affects the edge position in the XANES region and would lead to a higher uncertainty in LCF analysis.

The calculated average Fe oxidation state of the pristine MEA at each cell voltage is shown in Figure 6c (in blue, right y-axis), superimposed to the CV (same as the BoT results shown in Figure 5). The average Fe oxidation state ranges between ≈2.55 at a cell voltage above 0.8 V and ≈2.25 at a cell voltage below 0.6 V, showing a drastic decrease between ≈0.85 and ≈0.6 V, with a midpoint at ≈0.75 V, and a good agreement with the Fe redox peaks in the CV. It is noted that in our calculation, the highest oxidation state (i.e., ≈2.55 above 0.8 V) is lower than what was reported by Osmieri *et al.* (≈2.85 above ≈0.9 V). One possible reason for this discrepancy could be a significant difference in the coordination environment of the $Fe–N_4$ sites between the here examined catalyst and that studied in Osmieri *et al.*, which could lead to a difference in the average Fe oxidation state. This, however, seem unlikely, because it is not accompanied by a significant difference in the XANES spectra at the edge. Therefore, a more likely reason would be the leaching of iron ions (i.e., demetalation) during the ink preparation or the warm-up step (i.e., prior to the degradation test), followed by their coordination to the SO_3^- groups of the ionomer. The leached iron cations would quickly equilibrate in the ionomer phase of the entire MEA (electrodes and membrane) during the warm up step (H_2/N_2 configuration at 90% RH without any load), due to the fast diffusion of cations in the ionomer phase over the short distance across cathode/membrane/anode (≈100 μm; based on the reported diffusion coefficient of Ce^{3+} of $\approx 1 \cdot 10^{-5}$ $cm^2 s^{-1}$ in a fully humidified Nafion membrane at 80 °C,[49] equilibration across the MEA would require only $\approx 10^3$ s). While iron cations exchanged into the cathode ionomer would remain Fe^{3+} when the cell voltage (≡cathode potential vs. RHE) is above ≈0.75 V, those in the anode and in the membrane are preferentially reduced to Fe^{2+} due to the presence of cross-over H_2, thus sitting at a potential of ≈0 V vs. RHE. As the membrane can host more iron cations compared to the cathode due to its much higher overall ionomer content (i.e., ≈8.2 $\mu mol_{SO3^-} cm^{-2}_{MEA}$ in the membrane vs. ≈2.4 $\mu mol_{SO3^-} cm^{-2}_{MEA}$ in the cathode), the average iron oxidation state in the MEA will be reduced in the presence of significant amounts of leached iron ions, even when the cell voltage is above 0.75 V; thus, since the XAS measurements are probing the entire MEA, the XAS signal would also include the contributions from Fe^{2+} in the membrane, leading to a lower average iron oxidation state. As good representation of Fe^{2+} and Fe^{3+} coordinated to SO_3^- group in the ionomer,[50] we further plot the reference spectra of $FeSO_4$ (aq) (blue line) in Figure 6a, digitalized from reference[24] that reports spectra of 0.5 M sulphate solutions. The edge position of $FeSO_4$ (aq) is at an even lower energy than FeO, which would lead to a further underestimation of the average Fe oxidation state in the pristine MEA that we had calculated from the above XANES data.

Based on this analysis of the average Fe oxidation state as a function of cell voltage, the here used testing procedure (as reported in Figure 11) is designed to collect XANES data at two cell voltages, namely 0.9 V and 0.6 V, aiming to control the Fe oxidation state at the cathode in order to discriminate the Fe ions in the cathode from those ion-exchanged into the ionomer phase of the MEA over the course of the constant-voltage stability test.

XANES Spectra Over the Course of the H_2/O_2@0.8 V Stability Test

Figure 7a and b show the XANES spectra at Fe K-edge recorded under H_2/N_2 configuration at 0.9 V (high oxidation state) and 0.6 V (low oxidation state). Those spectra were collected at BoT and during the stability test H_2/O_2@0.8 V after 10 (in green), 30 (in purple), 105 (in red), and 180 minutes (denoted as EoT, in blue). After 10 minutes of the H_2/O_2@0.8 V stability test, the XANES spectra at the Fe K-edge recorded at 0.6 V and 0.9 V remain similar to those at BoT (comparison between black and green lines, Figure 7a and b). Additionally, their edge positions (shown in the insets Figure 7c and d for 0.9 V and 0.6 V, respectively) are very close, indicating only a marginal change of the Fe oxidation state. Considering the spectra after 30, 105 and 180 minutes (EoT), a gradual shift in edge position toward higher energy can be observed (Figure 7c and d), suggesting a gradual increase of the average Fe oxidation state over the course of the H_2/O_2@0.8 V stability test.

With the aim of finding the Fe species that predominantly lead to the XANES changes in Figure 7a–d, we first hypothesize that demetalation is the degradation mechanism during the H_2/O_2@0.8 V stability test, and that the leached iron cations

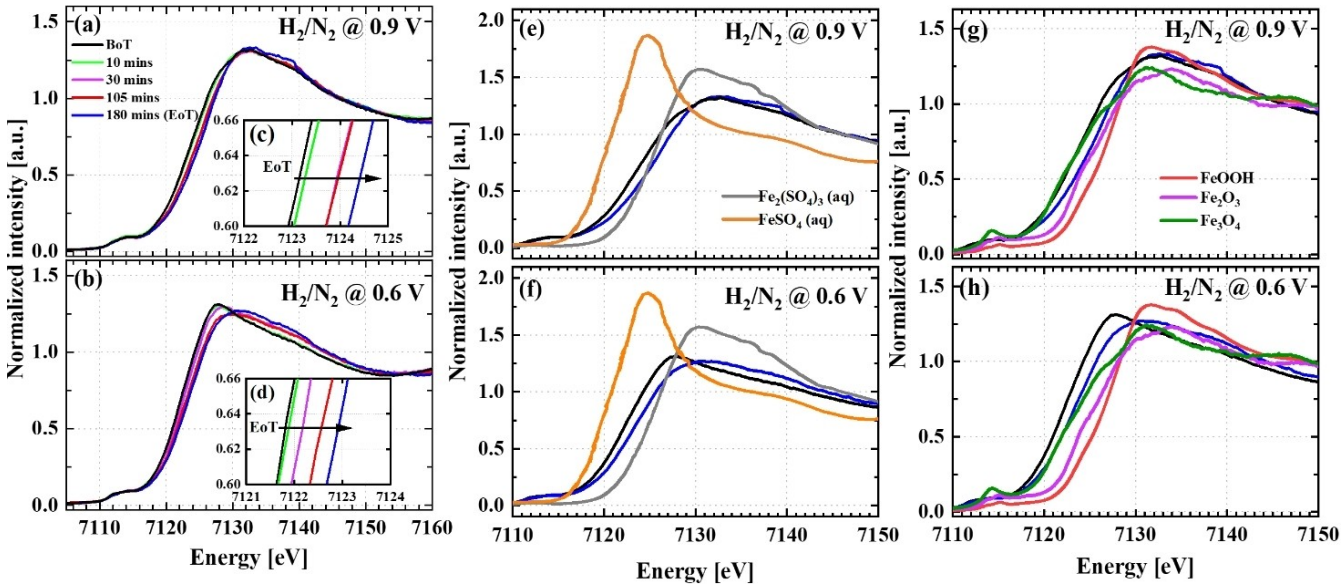

Figure 7. (a) and (b): XANES spectra at the Fe K-edge collected in H_2/N_2 configuration (anode/cathode, both at 400 nccm) at 90% RH, 80 °C, and 150 $kPa_{abs,inlet}$, acquired at 0.9 V and 0.6 V, respectively, over the course of the H_2/O_2@0.8 V stability test. The data collections occurred at BoT (in black), after 10 (in green), 30 (in purple), 105 (in red), and 180 minutes (in blue, EoT). (c) and (d) Detailed views of the edge positions from the results in (a) and (b), respectively. (e) and (f) Comparison of BoT and EoT spectra to the standard reference data for $FeSO_4$ (aq) (orange) and $Fe_2(SO_4)_3$ (aq) (gray; digitalized from reference 24 and also shown in Figure 6a). (g) and (h): Comparison of BoT and EoT spectra to the standard reference for Fe oxides,[34,36] namely FeOOH (red), Fe_2O_3 (purple), and Fe_3O_4 (green). The XAS data acquisition times are marked by the arrows in Figure 3.

coordinate to the SO_3^- groups of the ionomer across the whole MEA. Figure 7e and f report the spectra at BoT (in black) and EoT (in blue) together with the reference spectra of $FeSO_4$ (aq) (orange) and $Fe_2(SO_4)_3$ (aq) (gray), digitalized from reference[24] and also shown in Figure 6a (plotting $FeSO_4$ (aq)), which are very comparable to spectra of iron cations coordinating to SO_3^- in Nafion.[50] As already mentioned, if iron ions are leached out of the catalyst, they will quickly diffuse into the membrane and anode under H_2/N_2 at 90% RH and 80 °C (conditions chosen while recording XAS), equilibrating in the ionomer phase of the entire MEA. Therefore, as discussed for Figure 5c, a significant amount of iron cations in the membrane/anode side will be Fe^{2+} (comparable to $FeSO_4$ (aq)) due to the presence of H_2 (Fe ions being reduced), while they would be Fe^{3+} in the ionomer phase of the cathode, that are oxidized under the presence of O_2 (comparable to $Fe_2(SO_4)_3$ (aq)). In this case, the EoT spectrum recorded at 0.9 V under H_2/N_2 (blue in Figure 7e) would be expected to shift to lower energy (closer to the reference $FeSO_4$ (aq), orange line). However, this is apparently not the case, as the EoT spectrum in Figure 7e instead shifts to higher energy (toward $Fe_2(SO_4)_3$ (aq), gray line). Similarly, while recording the spectra at 0.6 V under H_2/N_2, all the iron cations in the ionomer phase should be Fe^{2+}, together with the iron species at the cathode electrode (when polarized to < 0.75 V), leading to the same expectation of an EoT XANES spectrum closer to $FeSO_4$ (aq). However, this expectation is also contradicted by the result shown in Figure 7f, as the edge position of the EoT spectrum (blue line) shifts to higher energy and oxidation state, closer to $Fe_2(SO_4)_3$. It is important to mention that, based on the above discussion, we do not exclude a partial reduction of iron cations in the ionomer at the EoT, but rather, we want to point out that it is not the major effect during the H_2/O_2@0.8 V stability test.

Since the EoT spectra (shown in Figure 7e and f) do not support the mechanism of accumulating leached iron ions in the ionomer phase, we evaluate the possible formation of Fe oxide precipitates during the H_2/O_2@0.8 V test. Previously, Li *et al.* reported that the demetalation of iron cations from the active sites initially results in their coordination with SO_3^- groups in the ionomer phase, followed by the formation of Fe_2O_3 nanoclusters upon extended exposure to air.[23] To check this hypothesis, Figure 7g and h compare BoT (black) and EoT (blue) spectra with three different Fe oxide references, namely FeOOH (red), Fe_2O_3 (purple), and Fe_3O_4 (green). The shift to higher energy of the edge position of the EoT spectra (blue line), regardless of the recording voltage (0.6 V or 0.9 V in H_2/N_2), fully agrees with the increasing presence of those Fe oxides, which are not in electronic contact with the carbon support in the cathode electrode but are located where they are not polarizable. This is also in agreement with their formation from the iron cations in the ionomer phase, which can electronically insulate them. The chance of precipitation of Fe oxide particles at the carbon, large enough to be at least partially insulated, sounds unlikely. More likely is their precipitation at the ionomer phase and at its interface with water.

To provide additional evidence and insight on our hypothesis, we also performed linear combination fits on the EoT spectra, combining the BoT spectra with either one of the three different Fe oxide references or a combination of them.

The best fits are obtained using the FeOOH spectrum, also yielding the lowest R-factor (reported in Table A2 for each fitting). A good agreement between LCFs with the FeOOH

spectrum and the EoT spectra is obtained for the spectra acquired under H_2/N_2 at both 0.9 V and 0.6 V, as evident from the low residual signals left after the fittings (gray lines in Figure 8). This analysis provides a rough estimate of the percentage of demetalation referenced to the total amount of Fe due to Fe(III) oxide precipitation (using the LCF with the FeOOH spectrum), yielding ≈31 and ≈37% for the data recorded at 0.6 and 0.9 V, respectively (see Table A2). It should be noted that we do not exclude other Fe oxides possibly formed at EoT, but the LCF analysis shown provides a high probability of growing mainly FeOOH over the course of the H_2/O_2@0.8 V stability test.

To justify the formation of Fe oxides during PEMFC operation, one should consider the concentration of iron cations in the ionomer phase, the local pH at the cathode electrode governed by the displacement of H^+ in the ionomer phase by Fe^{z+} ions, and the operating current density of the cell. The formation of $Co(OH)_2$ in the cathode of a Co^{2+} contaminated MEA based on Pt/C or Pt_xCo catalysts in a PEMFC was already reported in the literature.[10,51,52] There it was suggested that the migration flux of Co^{2+} ions to the cathode at high current density leads to a Co^{2+} ion enrichment in the ionomer phase of that electrode, displacing the H^+ in the cathode ionomer phase and thus increasing its pH to the point where $Co(OH)_2$ precipitation can occur.[52] Based on recent measurements, this appears to occur at current densities beyond ≈1 A cm^{-2}_{MEA} for Pt/C based MEAs with only ≈5–10 μm thick electrodes.[53]

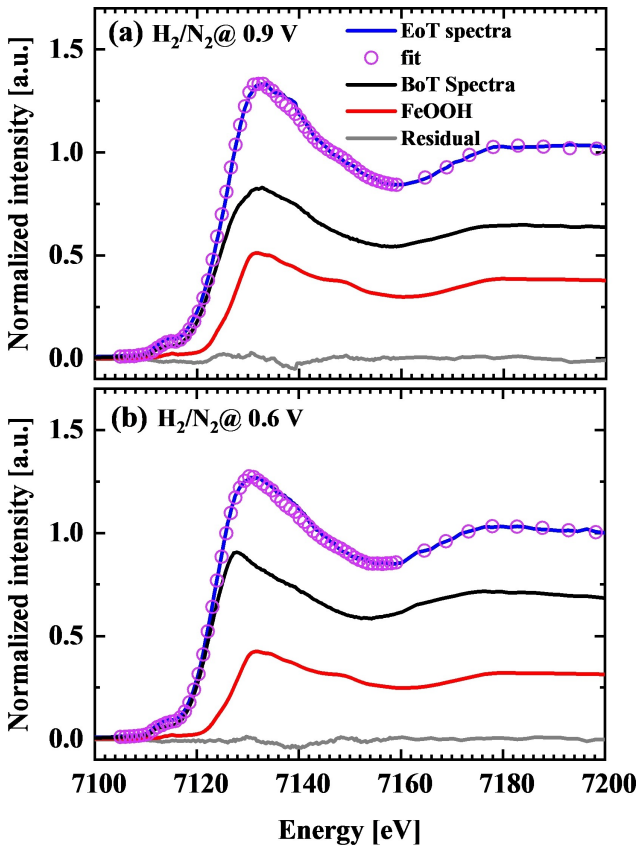

Figure 8. Results of the LCF on the EoT spectra of the H_2/O_2@0.8 V test (blue, as in Figure 7) recorded under H_2/N_2 at 0.9 V (a) and 0.6 V (b), using a combination of the spectrum at BoT (black line, as in Figure 7) and of the spectrum of FeOOH (red line). The purple circles represent the LCF curve, while the gray line is the residual signal after subtracting the LCF from the measured spectrum.

Since the operating current density is substantially lower during the H_2/O_2@0.8 V test shown in Figure 3a (≈5–30 mA cm^{-2}_{MEA}), at first glance one would not expect gradients in the concentration of dissolved iron ions. Here, however, it needs to be considered that for the very thick PGM-free catalyst-based MEAs in our study (≈100 μm), the back-diffusion rate of Fe^{z+} ions in the ionomer phase would be at least an order of magnitude slower, so that it is possible that even at the much lower current density, a significant enrichment of Fe^{z+} ions in the cathode electrode ionomer phase near the cathode/GDL interface could occur. Therefore, in the presence of a significant Fe demetalation during the H_2/O_2@0.8 V test, the local concentration of Fe^{z+} ions and thus the local pH could increase to the point where Fe oxides can precipitate. Additionally, once the Fe^{z+} ions precipitate as Fe oxides, their concentration in the ionomer phase of the cathode would be reduced, resulting in a decrease of their back-diffusion rate. By taking the amount of precipitated iron oxide estimated from the LCF analysis (≈35% FeOOH, see Table A2) and the total amount of Fe in the catalyst (for 2.7 wt% Fe content and a loading of 3.5 mg_{cat} cm^{-2}_{MEA}, this corresponds to ≈95 μg_{Fe} cm^{-2}_{MEA} or ≈1.7 μmol_{Fe} cm^{-2}_{MEA}), the amount of Fe initially leached into the ionomer phase over the course of the H_2/O_2@0.8 V test would be ≈0.6 μmol_{Fe} cm^{-2}_{MEA}. Considering dissolved iron ions at 0.8 V would be Fe^{3+} ions, this could replace ≈1.8 μmol_{H+} cm^{-2}_{MEA}, which would be ≈75% of the H^+ in the cathode ionomer phase at the above calculated SO_3^- loading of ≈2.4 μmol_{SO3} cm^{-2}_{MEA}. This creates a scenario where a significant increase of the local pH could enable the formation of Fe oxides in the cathode during the H_2/O_2@0.8 V test. It should be noted that to calculate the exact local pH and iron cation concentrations in the cathode ionomer would require an accurate modelling study, since it is a dynamic process involving the equilibrium between the leaching rate (demetalation rate) of iron cations, their migration and back-diffusion, as well as the precipitation rate of iron oxides, which is beyond the scope of this work. In principle, during the in situ XAS measurements under H_2/N_2 (i.e., in the absence of current and thus of Fe^{z+} migration), any Fe^{z+} ion concentration gradients and thus any H^+ or pH gradients would vanish, so that precipitated Fe oxides would dissolve,[54] unless the dissolution process is kinetically hindered. Furthermore, the decrease in the overall concentration of dissolved Fe species (also of Fe^{2+} in contact with H_2) upon precipitation is in total agreement with the LCF results after degradation. The presence of Fe^{2+} in the pristine MEA, evident and accounted for (see Figure 6), is not in contradiction with the LCF evidences after degradation but, on the contrary, fortifies them.

A further important remark is that we observed a significant performance loss already after ≈30 minutes of the H_2/O_2@0.8 V test (see the result in Figure 3), while, however, the change in shape of the XANES spectrum after 30 minutes is indeed very

small (see Figures 7a–d). This observation suggests that the utilization of the Fe–N_4 sites in our catalyst is very low, despite having ≈2.7 wt% of Fe in the pristine catalyst powder, of which 90% are Fe–N_4 sites (see Table 1). From this we can conclude that small losses of accessible Fe–N_4 sites from the catalyst result in significant performance losses (ORR activity) in the PEMFC.

XANES Spectra Over the Course of the H_2/O_2 @ 0.4 V Stability Test

Figure 9a and b report the XANES spectra at the Fe K-edge collected under H_2/N_2 configurations at the cell voltage of 0.9 V and 0.6 V, respectively, acquired over the course of the H_2/O_2@0.4 V stability test, namely at BoT (black), and after 10 (green), 30 (purple), 105 (red), and 180 minutes (blue, EoT). In contrast to the spectra in Figure 7 (from the H_2/O_2@0.8 V stability test), the edge positions of the spectra show a much smaller shift to higher energy (evident in the zoomed-in views in Figure 9c and d, plotted at the same scales as Figure 7c and d), particularly for the XANES data collected at 0.6 V. Additionally, it can be noticed that the intensity of the strongest peak (the so-called white line) gradually increases for the spectra recorded at both 0.9 V and 0.6 V, suggesting that the main degradation mechanism and the main decomposition products are different for the H_2/O_2@0.4 V versus the H_2/O_2@0.8 V stability test.

In analogy to the above discussion of the results for the H_2/O_2@0.8 V stability text, we examine the BoT and EoT spectra for the H_2/O_2@0.4 V stability test by comparing them with reference samples to elucidate the formation of possible Fe species at EoT. Figure 9e and h show the comparison with reference spectra for $FeSO_4$ (aq) (in orange) and $Fe_2(SO_4)_3$ (aq) (in gray), which considers the possibility of Fe demetalation and its coordination to the SO_3^- groups of the ionomer (showing very similar XANES spectra[50]). As already mentioned, under the conditions used during XAS data collection, the iron cations would ion-exchange into the ionomer phase in the electrodes and the membrane. If ion-exchange were to occur, most of the iron cations would be in the membrane (due to its highest ionomer content) and would be reduced to Fe^{2+} due to the presence of cross-over H_2. Consequently, the expected XANES spectra would shift toward $FeSO_4$ (aq). Nevertheless, as the edge position shifts slightly to higher energy over the course of the H_2/O_2@0.4 V test, regardless of the cell voltage applied during spectrum acquisition in H_2/N_2 (0.6 or 0.9 V), we can conclude that the major degradation mechanism cannot be the Fe demetallation of the catalyst followed by ion-exchange of leached iron ions into the ionomer phase. On the other hand, Figure 9g and h examine the possible formation of Fe oxides over the course of the H_2/O_2@0.4 V test, namely of FeOOH (red), Fe_2O_3(purple), and Fe_3O_4 (green). A similar argument to that used to described in Figure 7e and f can be used, from the observation of only a very small shift of the edge position between EoT and BoT spectra. Since those Fe oxides exhibit a higher oxidation state (i.e., edge position at higher energies), we can conclude that the changes in the spectra upon testing in H_2/O_2@0.4 V can at most marginally and not mainly be ascribed to Fe demetalation followed by Fe oxide formation.

The main change in the spectra over the H_2/O_2@0.4 V stability test is the intensity increase of the white line over time,

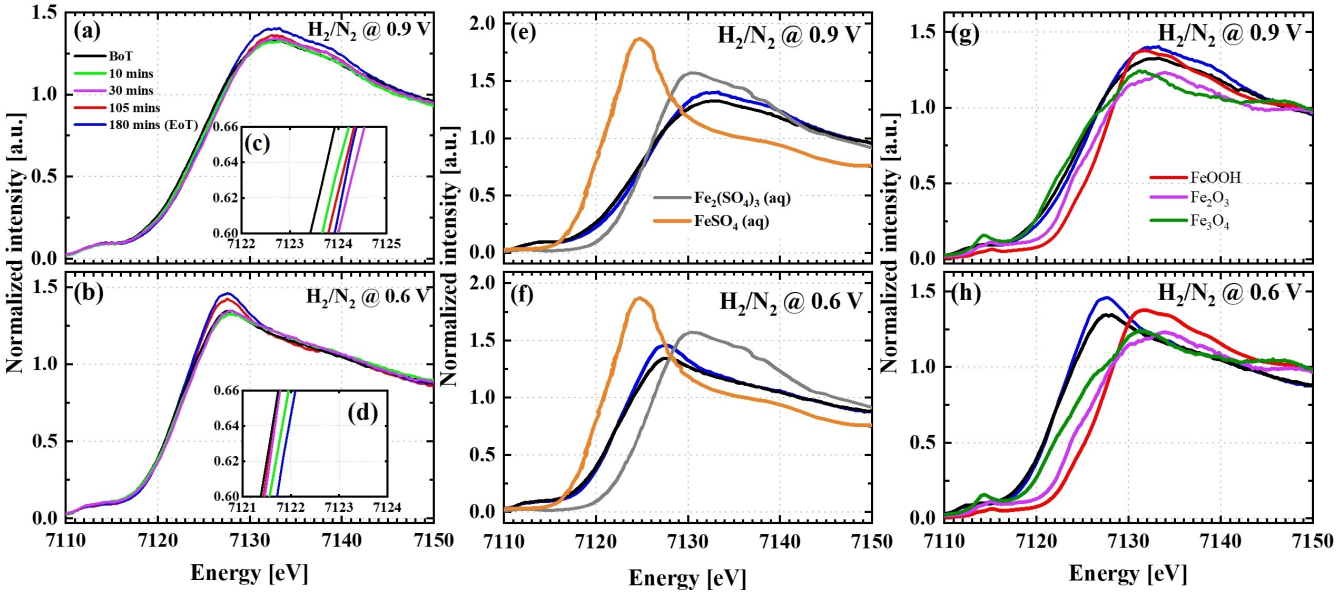

Figure 9. (a) and (b): XANES spectra at the Fe K-edge collected in H_2/N_2 configuration (anode/cathode, both at 400 nccm) at 90% RH, 80 °C, and 150 $kPa_{abs,inlet}$, acquired at 0.9 V and 0.6 V, respectively, over the course of the H_2/O_2@0.4 V stability test. The data collection occurred at BoT (in black), after 10 (in green), 30 (in purple), 105 (in red), and 180 minutes (in blue, EoT). (c) and (d): Detailed views of the edge positions from the results in (a) and (b), respectively. (e) and (f): Comparison of BoT and EoT spectra to the standard reference sample for $FeSO_4$ (aq) (orange) and $Fe_2(SO_4)_3$ (aq) (gray, same as in Figure 6a). (g) and (h): Comparison of BoT and EoT spectra to the standard reference for Fe oxides, namely FeOOH (red), Fe_2O_3 (purple), and Fe_3O_4 (green). The XAS data acquisition times are marked by the arrows in Figure 3.

remaining at a similar peak position (see Figures 9a and b). In general, the white line is attributed to the intense dipole-allowed 1*s*→4*p* transition of the absorbing element, i.e., of Fe in our case. An increase in white line intensity suggests that less electrons are present in the 4*p* orbitals or that these orbitals decrease their energy level. This happens if the number of electron-withdrawing ligands around the absorbing atom increases, i.e., if the electron density is being pulled away from the probed element, and if there is hybridization between 3*d* (interacting with the ligands orbitals) and 4*p* orbitals, as evidently is the case for Fe compounds.[55,56] Another probable degradation mechanism for Fe–N–C catalysts, likely related to the unique changes in spectral features upon the H_2/O_2@0.4 V stability test, is the attack from reactive oxygen species (ROS)[17] produced during the ORR, which would result in a *chemical* carbon oxidation (note that for *electrochemical* carbon oxidation higher potentials are required). This hypothesis is consistent with the CV results at EoT, where an increase in the CV area at ≈0.6 V (quinone/hydroquinone redox) is observed (Figure 5b). Moreover, this degradation mechanism seems plausible at the lower cell voltage (i.e., the lower cathode potential) due to the higher current densities compared to that of the H_2/O_2@0.8 V test (see Figure 3) in combination with the higher H_2O_2 yield at 0.4 versus 0.8 V (see Figure A1). This mechanism could eventually also result in Fe demetalation upon the accompanied destruction of the carbon scaffold.[57,58] The minor energy shift of the Fe K-edge upon degradation can be related to this event, observable but evidently marginal over the 3 hours of the experiment.

How can the attack by ROS be linked to the observed XAS trend? Choi *et al.* showed that the oxidation of the carbon scaffold (regarded as functionalization by oxygen-containing groups) would result in a depletion of electrons from the Fe sites, resulting in a decrease in turn-over frequency (TOF) of the active site.[17] This would indeed result in an increase of the white line intensity, as also shown by Lim *et al.*[59] and Mun *et al.*[60] ROS attack could also result in a structural modification of the Fe–N_4 sites if it takes place directly at the Fe atoms[61] or at the carbon atoms in close proximity to the Fe–N_4 sites, in the same way that has been shown for Fe phthalocyanine.[62] The first case could suggest that the Fe–N_4 sites are being poisoned by oxygen-containing radicals and that their binding energy is too high to remove them even at a low potential, due to the reduced TOF induced by carbon oxidation.[17] The second case would involve the breaking of one or more Fe–N bonds,[63] resulting in a possible transformation from the Fe–N_4 structure to a FeN_2O_2-like structure with a lower activity,[64,65] accompanied by a loss of N atoms, possibly in the form of NH_3.[62,66] García *et al.* also showed that the degradation-induced N loss of Fe–N–C catalysts is more pronounced for N-pyrrolic sites (the sites coordinating the Fe in our catalyst) than for N–pyridinic sites.[66] Consistent with the XAS results, this would also result in an increase of the white line intensity due to the electron withdrawing effect of O atoms. Furthermore, in the case of partial direct ROS attack of the active site, the edge positions of the XANES data collected at 0.9 V in H_2/N_2 should shift to higher energy, which indeed is observed, even though it is not very prominent. A minor demetalation can also be the result of multiple direct ROS attacks of the active sites.

To obtain further evidence for the loss of N atoms from the catalyst after ROS attack, we conducted a simple experiment in which we stirred the catalyst in 0.05 M H_2SO_4 at 80 °C in the presence of a Fenton reagent ($H_2O_2 + FeSO_4$) to simulate the conditions in a PEMFC. After 24 h, we tested the presence of NH_4^+ ions in the solution using a qualitative analytical stripe-test, which gave a positive result (Figure A4). Moreover, after this test, the elemental analysis of the filtrated and washed catalyst showed a decrease of ≈4 wt% in N content, clearly supporting the hypothesized loss of N due to the ROS attack. This degradation mechanism further supports what had recently been reported for the degradation of Fe phthalocyanine during the ORR in acidic electrolyte, where an attack by $^{\bullet}OH$ radicals, followed by NH_3 loss was proposed.[62] Although this simple qualitative experiment is not enough to conclusively prove that ROS attack is resulting in a restructuring of the Fe–N_4 sites, requiring further investigations to unravel the exact pathway, it is clear that the main degradation mechanism taking place over the course of the H_2/O_2@0.4 V stability test is mainly related to ROS attack, which can be mitigated by the addition of radical scavengers.[61] A secondary (stable) active site, which reduces very efficiently H_2O_2, close neighboring the Fe–N–C sites, could prevent the attack to the vicinal carbons, thus Fe–N–C deactivation at 0.4 V.

The EoT ORR activity after the H_2/O_2@0.4 V stability test is essentially identical with that observed after the H_2/O_2@0.8 V test (see Figure 4). This would be consistent with the degradation of most of the D1 sites (see Table 1) over the 3-hours stability test in H_2/O_2, so that the remaining catalyst activity would only be due to the more stable but less active D2 sites.

Conclusions

In this work, two different degradation protocols were used to evaluate the stability of a Fe–N–C ORR catalyst in a PEMFC operated with H_2/O_2 (80 °C, 90% RH), namely at 0.8 V and 0.4 V for 3 hours. The PEMFC results show that the two cases exhibit a similar current loss profile, with a fast decay within the first ≈ 30 min followed by a slower degradation. After operating the cell at 0.8 V for 3 h, a ≈80% loss in geometrical current density is observed, while it is only ≈50% upon operation at 0.4 V. Nevertheless, after these 3 h tests, the ORR activity determined at 0.8 $V_{HFR\text{-}free}$ is similar for both cases, decreasing by ≈90% of the initial activity. These results suggest that, independently of the protocol employed, most of the active sites have degraded in the 3 hours of the tests under H_2/O_2 and, after this time, only the most stable sites are contributing to the activity of the catalyst.

XANES spectra were acquired over the course of these stability tests, intermittently changing the gas feeds from H_2/O_2 to H_2/N_2 (anode/cathode) in order to avoid any catalyst degradation during the spectral acquisition time. They were recorded at either 0.6 or 0.9 V (80 °C, 90% RH) to elucidate the degradation mechanism, showing that upon H_2/O_2 operation at

0.8 V part of the Fe sites gradually increase their oxidation state and that this oxidized Fe fraction is not reducible after cell polarization at low potential. From this observation we can conclude that part of the Fe undergoes demetalation. Furthermore, performing a linear combination fitting (LCF) of the EoT spectra, based on a combination of the BoT spectrum and a FeOOH reference spectrum, we estimate that ≈35% of the total Fe contained in the catalyst is precipitated as Fe (III) oxide. Upon H_2/O_2 operation at 0.4 V, the irreversible increase of the average Fe oxidation state is barely observable, thus a direct demetalation cannot be the major degradation mechanism. On the other hand, an increase of the white line of the XANES spectra over the course of the H_2/O_2 operation at 0.4 V can be related to an attack to the carbon matrix in the vicinity of the active sites by reactive oxygen species (ROS), increasing the electron withdrawal from the Fe catalytic sites. This conclusion is also supported by an increase of the quinone/hydroquinone feature at ≈0.6 V in the CV at EoT. A direct ROS attack of the $Fe–N_4$ sites, possibly followed by a minor Fe demetalation, is also possible, as demonstrated by detecting NH_4^+ after *ex situ* chemical degradation of the pristine catalyst by ROS.

By employing constant potential measurements under H_2/O_2 and by probing the oxidation state of Fe under H_2/N_2, we are here able to disentangle different degradation mechanisms happening in a Fe–N–C electrocatalyst upon realistic operating conditions in an actual PEMFC. We believe that this work will help future research efforts aimed at improving the mechanistic understanding of the degradation of Fe–N–C catalysts and at developing more stable materials.

Experimental Section

Catalyst Synthesis

All commercially available chemicals were used without further purification. The porous and conductive commercial carbon Ketjenblack (KB) was used as support on which catalytically active Fe–N–C was deposited. In the following, the composite material is referred to as catalyst. In a typical synthesis, 1 g of KB (E-Type carbon, Tanaka Kikinzoku Kogyo K.K., Japan) was mixed with 1.3 g of $ZnCl_2$ (anhydrous, ≥98%, Sigma Aldrich, Germany) and 1.3 g of 1-ethyl-3-methylimidazolium dicyanamide (Emim-dca, >98%, Iolitech, Germany) in an Ar-filled glovebox (MBraun, Germany). The resulting mixture was placed inside an alumina crucible covered with a quartz lid and heated up to 850 °C for 1 h in a tube furnace (HTM Reetz, LK 1300-150-600-3, Germany) under a constant Ar 5.0 (99.999%, Westfalen AG, Germany) flow of 2 L min^{-1}, after an initial heating rate of 2.5 °C min^{-1}. After letting the sample naturally cool down to room temperature, it was ground and washed with 0.1 M HCl (prepared from concentrated 37 wt% HCl, Sigma Aldrich, Germany) for several hours. The Zn–N–C sample was then filtered and washed with deionized water until neutral pH was reached, then dried at 80 °C overnight. The material was subsequentially degassed at 250 °C under vacuum in a glass oven (B-585, Büchi, Switzerland) and mixed with an eutectic mixture of $FeCl_3$/LiCl (97% and 99%, respectively, from Sigma Aldrich, Germany, 4.13 mass ratio) inside an Ar-filled flask in order to exchange the zinc cations in the Zn–N–C materials with iron cations.[36] After stirring at 170 °C for 5 h in the molten salt mixture, the sample was first washed with deionized water to remove the salts, then stirred in 0.1 M HCl for ≈12 hours. The powder obtained after further water washing until neutral pH and drying overnight was placed again in an alumina crucible and pushed inside a tube furnace that was pre-heated at 800 °C under Ar atmosphere (flash pyrolysis). After 20 minutes, the furnace was turned off and opened to quickly cool down the sample. The Fe content in the sample is 2.7 wt% as determined by ICP-MS measurements. The surface area of the catalyst (446 m^2 g^{-1}) was evaluated with N_2-sorption porosimetry (performed on an Autosorb iQ2 by Quantachrome, USA). Brunauer–Emmett–Teller (BET) theory was employed to determine the specific surface area using the Micropore BET Assistant provided in the Quantachrome AsiQwin software.

Mössbauer Spectroscopy

Mössbauer measurements at a temperature of 4.2 K were performed employing a standard transmission spectrometer using a sinusoidal velocity waveform, with both the source (^{57}Co in rhodium) and the absorber immersed in the liquid-He bath of a cryostat. To refer the measured isomer shifts to α–Fe at ambient temperature, 0.245 mm s^{-1} was added to the measured values.

Rotating Ring Disk Electrode (RRDE) Measurements

Catalyst inks were prepared by dispersing 5 mg of catalyst in 0.84 mL of Milli-Q water (Merck Millipore, Germany), 1.68 mL of isopropanol, and 50 μL of 5 wt% Nafion suspension, followed by bath sonication for 1 h. To obtain a catalyst loading of 0.1 mg cm^{-2}, 10 μL of ink were drop-cast onto a well-polished glassy carbon electrode (Pine Research Instrumentation, USA) and dried under an infrared lamp for 60 min. The obtained electrodes were measured in a three-electrode glass cell using 0.1 M $HClO_4$ as electrolyte, Au wire as the counter electrode, and a freshly calibrated reversible hydrogen electrode (RHE) as the reference electrode. The RHE was prepared by passing a negative current on the Pt wire immersed in 0.1 M $HClO_4$ solution contained inside the electrode compartment in order to evolve H_2. A 60 wt% $HClO_4$ solution (>99%, Guaranteed Reagent, Kanto Chemical, Japan) was used to prepare 0.1 M $HClO_4$ solution. The dilution was performed with deionized ultrapure water (Milli-Q Integral 5, 18.2 MΩ cm). The uncompensated resistance of the electrolyte solution was determined by electrochemical impedance spectroscopy. The ORR current was corrected for capacitive contributions by subtracting from the data recorded in O_2-saturated electrolyte the current recorded in Ar-saturated electrolyte. The H_2O_2 production of the catalyst was quantified on the Pt ring electrode, which was held at 1.2 V_{RHE}, while the potential of the disk was swept between 1.0–0.1 V_{RHE}. The collection efficiency of the ring (N) was calculated from the ring-disk geometry to be 0.255[67,68] and the fraction of H_2O_2 was calculated using equation 1:

$$H_2O_2\% = \frac{2\ i_R/N}{i_D + i_R/N} \quad (1)$$

where i_R and i_D represent the current measured at the ring and at the disk, respectively.

Membrane Electrode Assembly (MEA) Preparation and Single-Cell PEMFC Assembly

Prior to ink preparation, the PGM-free catalyst powder was dry ball-milled using a 20 mL ZrO_2 milling-vessel with 10 ZrO_2 beads of 10 mm diameter (corresponding to a 30/1 beads/catalyst mass

ratio) at 200 rpm for 90 min (planetary ball mill: Pulverisette 7, Fritsch, Germany). The cathode catalyst ink was then prepared by mixing the ball-milled powder, the ionomer solution (≈25 wt% of a low equivalent weight EW≈700 in water, Asahi Kasei, Japan), the solvent mixture of 1-propanol/H_2O (27 wt% of H_2O in 1-propanol), and 15 ZrO_2 beads of 3 mm diameter (corresponding to ≈15/1 beads/catalyst mass ratio) in an ARV-310 planetary mixer (Thinky, USA) at 500 rpm for 10 min using a 20 mL vial. The catalyst ink had a carbon content of 0.065 g mL_{ink}^{-1} and an ionomer/carbon ratio (I/C, wt/wt) of 0.5/1. The catalyst ink was then coated on a PTFE substrate (thickness: 50 μm, APSOparts, Germany) using a gap-bar with 500 μm wet-film thickness and was dried under ambient condition, targeting ≈3.5 $mg_{cat}cm^{-2}_{MEA}$ and a thickness of ≈100 μm. The anode electrode was prepared with the method reported previously,[34,46,69] using a commercial Pt/C catalyst (19.6 wt% Pt on Vulcan carbon support, TEC10 V20E, Tanaka Kikinzoku Kogyo K.K., Japan). The ink was prepared by mixing the same ionomer (I/C = 0.65) with 1-propanol/H_2O mixture (10 wt% of H_2O content). The ink was coated on the same type of PTFE substrate to achieve ≈0.1 $mg_{Pt}cm^{-2}_{MEA}$ and a thickness of ≈10 μm. The MEA (having a geometrical electrode area of 5 cm^2) was then prepared using the catalyst–coated–membrane (CCM) method and the decal transfer technique, consisting in a hot-press procedure applied to a PEM (≈45 μm, Nafion 212, Fuel Cell Store, USA) sandwiched between anode and cathode decals at 130 °C and 4 kN for 10 minutes. The PTFE substrates were subsequently peeled off from anode and cathode sides of the MEA, yielding the final CCMs. The 5 cm^2_{MEA} single-cell PEMFCs employed at the beamline consist of an in-house-designed graphite flow field and a modified fuel cell hardware, previously reported in references.[34,70] The fuel cell hardware (Fuel Cell Technologies, Inc., USA) is modified by machining a conically shaped aperture for the X-rays, with the lowest part in the middle of the hardware (1.5×2.6 mm^2, see Figure 10a). The graphite flow field has a single-channel, single-serpentine design (single channel with 3 serpentines and 2.0/1.3 mm channel/land width and 1 mm channel depth, manufactured by Poco Graphite, USA) and a rectangular X-ray window in the middle, 0.5 mm thick to limit X-ray attenuation while preventing any gas permeation. The used gas diffusion layers (GDLs) were H14C10 (≈170 μm, Freudenberg, Germany) with a compression to get 13±1% of thickness reduction upon cell assembly. This GDL compression is controlled by adjusting the thickness of a PTFE-coated glass-fiber subgasket (Fiberflon) and by assembling at an applied torque of 12 N m (for further details see the paper from our group by Simon *et al.*).[71] A sketch of all the cell components is shown in Figure 10c (note that the illustration does not reflect real relative dimensions of each components).

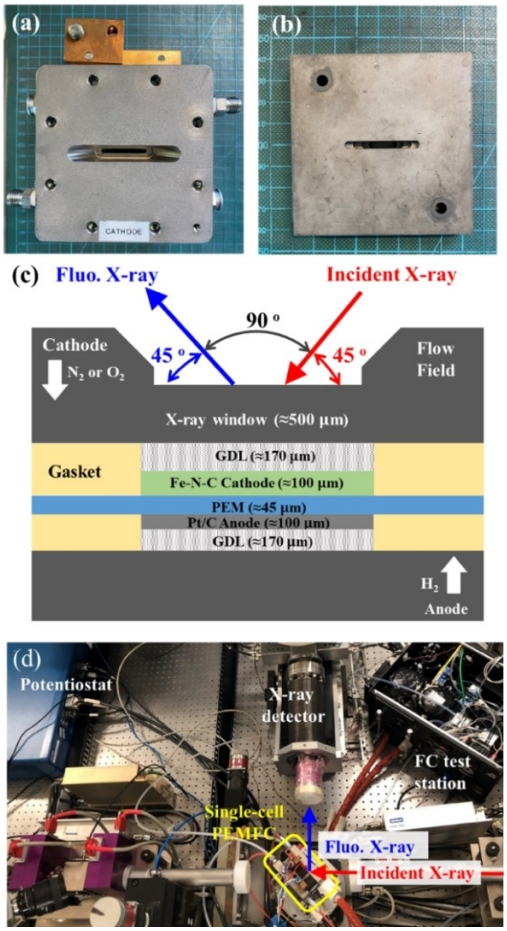

Figure 10. Photographs of the X-ray windows for XAS measurements on the cathode-side of the cell hardware (a) and of the corresponding flow field (b) employed for the *in situ* PEMFC tests. (c) Schematic representation of the cross-sectional cell assembly of the single-cell hardware and MEA for the *in situ* XAS measurements, indicating the thickness of each relevant component (note that the schematic representation does not reflect the actual relative dimension of each component). The incident X-ray beam (red arrow) is illuminating the MEA through a part of the graphite flow field thinned to ≈0.5 mm, with a 45-degree angle between beam and surface of the graphite window. The fluorescent X-ray beam from the sample (blue arrow) is collected at a 90- and 45-degree angle between the incident X-ray and the surface of the graphite window, respectively. (d) Top view photograph of the experimental setup employed at the BM30 beamline of the European Synchrotron Radiation Facility. The yellow rectangle indicates the single-cell hardware used in this study (i.e., the flow field and the assembly shown in (a), (b), and (c)). The fuel cell station, the potentiostat, and the X-ray detector collecting the X-ray fluorescence are located on the right side, left side, and upper part of the photograph, respectively.

Beamline Setup and PEMFC Measurements

The beamline setup for PEMFC tests for *in situ* XAS data collection is shown in Figure 10d. The gas flow, cell temperature, gas humidification, and gas pressure were controlled by a customized portable, semi-automated fuel cell test station (Fuel Cell Technologies Inc., USA, see upper right side of Figure 10d). All electrochemical measurements were performed with a VSP-300 multichannel potentiostat equipped with a 20 A booster board (Biologic SAS, France, see left side of Figure 10d). The fuel cell hardware (the yellow rectangle in Figure 10d) was placed by aligning the graphite window of the flow field with the incident X-ray beam (red arrow in Figure 10c and 10d), forming a 90-degree angle between incident and emitted fluorescence beams (blue arrow in Figure 10c and 10d) going into the detector (for more details see reference[34]). The sequence of fuel cell tests and *in situ* XAS measurements is sketched in Figure 11. All the PEMFC tests were performed at 90% relative humidity (RH), 80 °C, and 150 $kPa_{abs,inlet}$, using a flow of 400 nccm (normal cubic centimeters per minute, defined at standard conditions of 273.15 K and 101.3 kPa) for both anode and cathode. Prior to any fuel cell test, the cell was warmed up under a H_2/N_2 (anode/cathode) configuration for 15 minutes (gray box in Figure 11). Cyclic voltammograms (CVs) were recorded at BoT and EoT under a H_2/N_2 (anode/cathode) configuration, using a scan rate of 100 $mV s^{-1}$ (green box in Figure 11). Prior to the CV measurement, the cathode was purged with N_2 for 15 minutes to eliminate any residual oxygen. The XAS measurements (blue box in Figure 11) were conducted under H_2/N_2 (anode/cathode) at two cell voltages to control the oxidation state of the Fe species at the MEA, namely at 0.6 V (Fe^{2+}) and at 0.9 V (Fe^{3+}). The XAS spectra were recorded at BoT and followed every constant-voltage stability test after 10, 30,

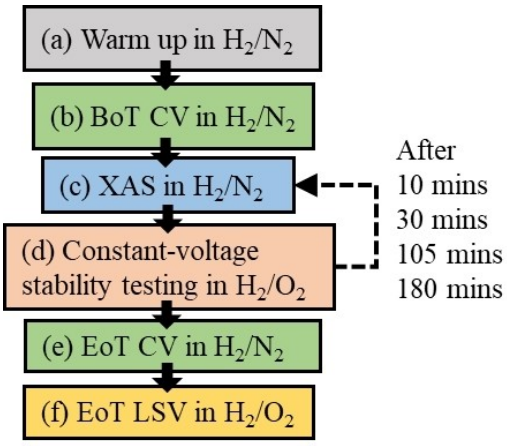

Figure 11. Schematic representation of the test protocol employed for testing catalyst stability and recording *in situ* XAS data. The detailed experimental conditions are described in the experimental section. The testing sequence is as follows: (a) warming up of the cell prior to the testing; (b) BoT cyclic voltametric (CV) measurement; (c) XAS data collection; (d) constant-voltage-stability test with a cell voltage of 0.4 and 0.8 V; (e) EoT CV measurement; and, (f) ORR activity determination of the catalyst at EoT via LSV. Step (c) is repeated after 10, 30, 105, and 180 minutes of step (d).

105, and 180 minutes (end-of-test, EoT). The stability tests (red box in Figure 11) were conducted at constant-voltage under H_2/O_2 (anode/cathode).

For these tests, two cell voltages (0.4 V and 0.8 V) were chosen for two reproduced fuel cells and held for 3 hours in total. Two sets of these experiments were carried out, one was performed at the European Synchrotron Radiation Facility, using the portable fuel cell test station for XAS *in situ* measurements; the other was performed using a Greenlight G60 fuel cell test station in our laboratory to validate the PEMFC results obtained at the synchrotron. This comparison followed the experimental design of a previous publication from our group.[34] The linear scan voltammetry (LSV, yellow box in Figure 11) was recorded at EoT only at a scan rate of 2 mV s^{-1} from OCV to 0.4 V under H_2/O_2 (anode/cathode). To correct the cell voltage for the ohmic drop, the high frequency resistance (HFR) was recorded after each LSV. This was performed using potentiostatic electrochemical impedance spectroscopy (PEIS) at a cell voltage of 0.6 V under the same conditions as the LSV, acquired from 200 kHz to 1 Hz with 10 mV voltage perturbation. The HFR was then derived from the Nyquist plot using the linear extrapolation of the 45-degree line to the real part of the impedance (x-axis of the Nyquist plot).

XAS Measurements

XAS spectra at the Fe K-edge were collected on the bending-magnet beamline CRG-FAME (BM30) at the European Synchrotron Radiation Facility (Grenoble, France). The beamline description can be found in reference[70] and,[34] where the same *in situ* cell was used. The ring was operated at 6 GeV with a nominal current of 200 mA in the uniform mode. The beamline was equipped with a liquid-nitrogen-cooled double-crystal Si (2 2 0) monochromator surrounded by two Rh-coated mirrors for harmonic rejection. For the Fe K-edge, the mirrors were set to 6 mrad to remove harmonics and photons with energy higher than ≈10 keV. The beam size was measured to be around 210 μm×100 μm (H x V, full width at half maximum values). The monochromator was energy calibrated at the Fe K-edge by setting the first maximum of the first derivative in the spectrum of metallic Fe to 7112 eV. *In situ* spectra were recorded in fluorescence mode using a Canberra 13-element Ge solid-state detector with a 45-degree angle between sample surface and beam (see Figure 10c), i.e., the incident X-ray (red arrow in Figures 10c and 10d) has a 90-degree angle with the fluorescence X-ray (blue arrow in Figures 10c and 10d). The spectra were collected between 7000 and 7960 eV, with 4 eV step and 2 s per step to 7080 eV, then 0.2 eV step and 2 s per step to 7180 eV and finally a constant 0.05 $Å^{-1}$ k-step and 2 s per step to 7960 eV. The beam damage was minimized by moving between four different spots while collecting consecutive spectra. Moreover, the possibility of MEA failure due to beam damage was tested collecting consecutive spectra on the same spot for 2 hours, similarly to reference.[34] No membrane failure was detected electrochemically, and no spectroscopic change was visible during this time. The Demeter software package was employed for normalization and processing of the collected X-ray Absorption Near Edge Structure (XANES) data.[72]

Acknowledgements

We would like to thank the support from European Union's Horizon 2020 Program (H2020) (Project: Pegasus, call JTI-FCH2017-1). PEGASUS has received funding from the Fuel Cells and Hydrogen 2 Joint Undertaking under grant agreement No 779550. This Joint Undertaking receives support from the European Union's Horizon 2020 research and innovation program, Hydrogen Europe and Hydrogen Europe research. We thank the European Synchrotron Radiation Facility (ESRF) and BM30 FAME beamline for providing beamtime (proposal MA-4587). Open Access funding enabled and organized by Projekt DEAL.

Conflict of Interests

The authors declare no conflict of interests.

Data Availability Statement

The data that support the findings of this study are available on request from the corresponding author. The data are not publicly available due to privacy or ethical restrictions.

Keywords: PEM fuel cell · Fe–N–C ORR catalyst · In situ XAS · Degradation · Stability

[1] F. Jaouen, D. Jones, N. Coutard, V. Artero, P. Strasser, A. Kucernak, *Johns. Matthey Technol. Rev.* **2018**, *62*, 231.
[2] A. Kongkanand, M. F. Mathias, *J. Phys. Chem. Lett.* **2016**, *7*, 1127.
[3] C. S. Gittleman, A. Kongkanand, D. Masten, W. Gu, *Curr. Opin. Electrochem.* **2019**, *18*, 81.
[4] S. T. Thompson, D. Papageorgopoulos, *Nat. Catal.* **2019**, *2*, 558.
[5] L. Jiao, J. Li, L. L. Richard, Q. Sun, T. Stracensky, E. Liu, M. T. Sougrati, Z. Zhao, F. Yang, S. Zhong, H. Xu, S. Mukerjee, Y. Huang, D. A. Cullen, J. H. Park, M. Ferrandon, D. J. Myers, F. Jaouen, Q. Jia, *Nat. Mater.* **2021**, *20*, 1385.
[6] A. Mehmood, M. Gong, F. Jaouen, A. Roy, A. Zitolo, A. Khan, M.-T. Sougrati, M. Primbs, A. M. Bonastre, D. Fongalland, G. Drazic, P. Strasser, A. Kucernak, *Nat. Catal.* **2022**, *5*, 311.

[7] X. Wan, X. Liu, Y. Li, R. Yu, L. Zheng, W. Yan, H. Wang, M. Xu, J. Shui, *Nat. Catal.* **2019**, *2*, 259.
[8] J. Weiss, H. Zhang, P. Zelenay, *J. Electroanal. Chem.* **2020**, *875*, 114696.
[9] R. K. Ahluwalia, X. Wang, J. K. Peng, V. Konduru, S. Arisetty, N. Ramaswamy, S. Kumaraguru, *J. Electrochem. Soc.* **2021**, *168*, 044518.
[10] N. Ramaswamy, S. Kumaraguru, R. S. Kukreja, D. Groom, K. Jarvis, P. Ferreira, *J. Electrochem. Soc.* **2021**, *168*, 124512.
[11] R. K. F. Della Bella, B. M. Stühmeier, H. A. Gasteiger, *J. Electrochem. Soc.* **2022**, *169*, 044528.
[12] D. Banham, T. Kishimoto, Y. Zhou, T. Sato, K. Bai, J.-i. Ozaki, Y. Imashiro, S. Ye, *Sci. Adv.* **2018**, *4*, eaar7180.
[13] L. Osmieri, D. A. Cullen, H. T. Chung, R. K. Ahluwalia, K. C. Neyerlin, *Nano Energy* **2020**, *78*, 105209.
[14] R. Chenitz, U. I. Kramm, M. Lefèvre, V. Glibin, G. Zhang, S. Sun, J.-P. Dodelet, *Energy Environ. Sci.* **2018**, *11*, 365.
[15] M. Ferrandon, X. Wang, A. J. Kropf, D. J. Myers, G. Wu, C. M. Johnston, P. Zelenay, *Electrochim. Acta* **2013**, **110**, 282.
[16] C. H. Choi, C. Baldizzone, J.-P. Grote, A. K. Schuppert, F. Jaouen, K. J. J. Mayrhofer, *Angew. Chem. Int. Ed.* **2015**, *54*, 12753.
[17] C. H. Choi, H.-K. Lim, M. W. Chung, G. Chon, N. Ranjbar Sahraie, A. Altin, M.-T. Sougrati, L. Stievano, H. S. Oh, E. S. Park, F. Luo, P. Strasser, G. Dražić, K. J. J. Mayrhofer, H. Kim, F. Jaouen, *Energy Environ. Sci.* **2018**, *11*, 3176.
[18] G. Zhang, R. Chenitz, M. Lefèvre, S. Sun, J.-P. Dodelet, *Nano Energy* **2016**, *29*, 111.
[19] G. Liu, X. Li, J.-W. Lee, B. N. Popov, *Catal. Sci. Technol.* **2011**, *1*, 207.
[20] Y. Shao, J.-P. Dodelet, G. Wu, P. Zelenay, *Adv. Mater.* **2019**, *31*, 1807615.
[21] X. Xu, X. Zhang, Z. Kuang, Z. Xia, A. I. Rykov, S. Yu, J. Wang, S. Wang, G. Sun, *Appl. Catal. B Environ.* **2022**, *309*, 121290.
[22] S. Liu, C. Li, M. J. Zachman, Y. Zeng, H. Yu, B. Li, M. Wang, J. Braaten, J. Liu, H. M. Meyer, M. Lucero, A. J. Kropf, E. E. Alp, Q. Gong, Q. Shi, Z. Feng, H. Xu, G. Wang, D. J. Myers, J. Xie, D. A. Cullen, S. Litster, G. Wu, *Nat. Energy* **2022**, *7*, 652.
[23] J. Li, M. T. Sougrati, A. Zitolo, J. M. Ablett, I. C. Oğuz, T. Mineva, I. Matanovic, P. Atanassov, Y. Huang, I. Zenyuk, A. Di Cicco, K. Kumar, L. Dubau, F. Maillard, G. Dražić, F. Jaouen, *Nat. Catal.* **2021**, *4*, 10.
[24] Y. Nabae, Q. Yuan, S. Nagata, K. Kusaba, T. Aoki, N. Takao, T. Itoh, M. Arao, H. Imai, K. Higashi, T. Sakata, T. Uruga, Y. Iwasawa, *J. Electrochem. Soc.* **2021**, *168*, 014513.
[25] K. Kumar, L. Dubau, F. Jaouen, F. Maillard, *Chem. Rev.* **2023**, *123*, 9265.
[26] K. Kumar, P. Gairola, M. Lions, N. Ranjbar-Sahraie, M. Mermoux, L. Dubau, A. Zitolo, F. Jaouen, F. Maillard, *ACS Catal.* **2018**, *8*, 11264.
[27] U. I. Kramm, M. Lefèvre, P. Bogdanoff, D. Schmeißer, J.-P. Dodelet, *J. Phys. Chem. Lett.* **2014**, *5*, 3750.
[28] V. Goellner, C. Baldizzone, A. Schuppert, M. T. Sougrati, K. Mayrhofer, F. Jaouen, *Phys. Chem. Chem. Phys.* **2014**, *16*, 18454.
[29] M. Lefèvre, J.-P. Dodelet, *Electrochim. Acta* **2003**, *48*, 2749.
[30] U. I. Kramm, L. Ni, S. Wagner, *Adv. Mater.* **2019**, *31*, 1805623.
[31] L. Ni, C. Gallenkamp, S. Wagner, E. Bill, V. Krewald, U. I. Kramm, *J. Am. Chem. Soc.* **2022**, *144*, 16827.
[32] L. Osmieri, R. K. Ahluwalia, X. Wang, H. T. Chung, X. Yin, A. J. Kropf, J. Park, D. A. Cullen, K. L. More, P. Zelenay, D. J. Myers, K. C. Neyerlin, *Appl. Catal. B Environ.* **2019**, *257*, 117929.
[33] Q. Jia, N. Ramaswamy, H. Hafiz, U. Tylus, K. Strickland, G. Wu, B. Barbiellini, A. Bansil, E. F. Holby, P. Zelenay, S. Mukerjee, *ACS Nano* **2015**, *9*, 12496.
[34] A. M. Damjanović, A. T. S. Freiberg, A. Siebel, B. Koyutürk, D. Menga, K. Krempl, P. Madkikar, O. Proux, H. A. Gasteiger, M. Piana, *ChemElectroChem* **2023**, *10*, e202300185.
[35] D. Menga, F. Ruiz-Zepeda, L. Moriau, M. Šala, F. Wagner, B. Koyutürk, M. Bele, U. Petek, N. Hodnik, M. Gaberšček, T.-P. Fellinger, *Adv. Energy Mater.* **2019**, *9*, 1902412.
[36] D. Menga, J. L. Low, Y.-S. Li, I. Arčon, B. Koyutürk, F. Wagner, F. Ruiz-Zepeda, M. Gaberšček, B. Paulus, T.-P. Fellinger, *J. Am. Chem. Soc.* **2021**, *143*, 18010.
[37] A. Mehmood, J. Pampel, G. Ali, H. Y. Ha, F. Ruiz-Zepeda, T.-P. Fellinger, *Adv. Energy Mater.* **2018**, *8*, 1701771.
[38] D. Menga, A. G. Buzanich, F. Wagner, T.-P. Fellinger, *Angew. Chem. Int. Ed.* **2022**, *61*, e202207089.
[39] T. Mineva, I. Matanovic, P. Atanassov, M.-T. Sougrati, L. Stievano, M. Clémancey, A. Kochem, J.-M. Latour, F. Jaouen, *ACS Catal.* **2019**, *9*, 9359.
[40] D. Menga, F. E. Wagner, T.-P. Fellinger, *Mater. Horiz.* **2023**, *10*, 5577.
[41] V. A. Saveleva, K. Kumar, P. Theis, N. S. Salas, U. I. Kramm, F. Jaouen, F. Maillard, P. Glatzel, *ACS Appl. Energy Mater.* **2023**, *6*, 611.
[42] G. Zhang, X. Yang, M. Dubois, M. Herraiz, R. Chenitz, M. Lefèvre, M. Cherif, F. Vidal, V. P. Glibin, S. Sun, J.-P. Dodelet, *Energy Environ. Sci.* **2019**, *12*, 3015.
[43] X. Yin, E. F. Holby, P. Zelenay, *Energy Environ. Sci.* **2021**, *14*, 1029.
[44] X. Yin, P. Zelenay, *ECS Trans.* **2018**, *85*, 1239.
[45] N. Macauley, D. D. Papadias, J. Fairweather, D. Spernjak, D. Langlois, R. Ahluwalia, K. L. More, R. Mukundan, R. L. Borup, *J. Electrochem. Soc.* **2018**, *165*, F3148.
[46] A. M. Damjanović, B. Koyutürk, Y.-S. Li, D. Menga, C. Eickes, H. A. El-Sayed, H. A. Gasteiger, T.-P. Fellinger, M. Piana, *J. Electrochem. Soc.* **2021**, *168*, 114518.
[47] A. Nicolellis, M. Newville, XrayDB Web App, in (2022).
[48] S. Gottesfeld, *ECS Trans.* **2014**, *61*, 1.
[49] F. D. Coms, A. B. McQuarters, *ECS Trans.* **2018**, *86*, 395.
[50] H. K. Pan, D. J. Yarusso, G. S. Knapp, M. Pineri, A. Meagher, J. M. D. Coey, S. L. Cooper, *J. Chem. Phys.* **1983**, *79*, 4736.
[51] Y. Cai, A. Kongkanand, W. Gu, T. E. Moylan, *ECS Trans.* **2015**, *69*, 1047.
[52] T. A. Greszler, T. E. Moylan, H. A. Gasteiger, in *Handbook of Fuel Cells*.
[53] N. Ramaswamy, S. Kumaraguru, W. Gu, R. S. Kukreja, K. Yu, D. Groom, P. Ferreira, *J. Electrochem. Soc.* **2021**, *168*, 024519.
[54] B. Beverskog, I. Puigdomenech, *Corros. Sci.* **1996**, *38*, 2121.
[55] P. Wernet, *Philos. Trans. Royal Soc. A Math Phys. Eng. Sci.* **2019**, *377*, 20170464.
[56] T. Kroll, M. L. Baker, S. A. Wilson, M. Lundberg, A. Juhin, M.-A. Arrio, J. J. Yan, L. B. Gee, A. Braun, T.-C. Weng, D. Sokaras, B. Hedman, K. O. Hodgson, E. I. Solomon, *J. Am. Chem. Soc.* **2021**, *143*, 4569.
[57] K. Kumar, L. Dubau, M. Mermoux, J. Li, A. Zitolo, J. Nelayah, F. Jaouen, F. Maillard, *Angew. Chem. Int. Ed.* **2020**, *59*, 3235.
[58] X. Tan, H. A. Tahini, S. C. Smith, *J. Mater. Chem. A* **2021**, *9*, 8721.
[59] W.-G. Lim, C.-Y. Park, H. Jung, S. Kim, S. H. Kang, Y.-G. Lee, Y. C. Jeong, S. B. Yang, K. Sohn, J. W. Han, J. Lee, *Adv. Mater.* **2023**, *35*, 2208999.
[60] Y. Mun, S. Lee, K. Kim, S. Kim, S. Lee, J. W. Han, J. Lee, *J. Am. Chem. Soc.* **2019**, *141*, 6254.
[61] H. Xie, X. Xie, G. Hu, V. Prabhakaran, S. Saha, L. Gonzalez-Lopez, A. H. Phakatkar, M. Hong, M. Wu, R. Shahbazian-Yassar, V. Ramani, M. I. Al-Sheikhly, D.-e. Jiang, Y. Shao, L. Hu, *Nat. Energy* **2022**, *7*, 281.
[62] L. Wan, K. Zhao, Y.-C. Wang, N. Wei, P. Zhang, J. Yuan, Z. Zhou, S.-G. Sun, *ACS Catal.* **2022**, *12*, 11097.
[63] N. Yang, L. Peng, L. Li, J. Li, Q. Liao, M. Shao, Z. Wei, *Chem. Sci.* **2021**, *12*, 12476.
[64] X. Yang, W. Sun, J. Chen, Y. Gao, R. Zhang, Q. Luo, T. Lyu, L. Du, *J. Mater. Sci. Technol.* **2024** *173*, 100.
[65] C. Tang, L. Chen, H. Li, L. Li, Y. Jiao, Y. Zheng, H. Xu, K. Davey, S.-Z. Qiao, *J. Am. Chem. Soc.* **2021**, *143*, 7819.
[66] Á. García, L. Pascual, P. Ferrer, D. Gianolio, G. Held, D. C. Grinter, M. A. Peña, M. Retuerto, S. Rojas, *J. Power Sources* **2021**, *490*, 229487.
[67] P. Madkikar, D. Menga, G. S. Harzer, T. Mittermeier, A. Siebel, F. E. Wagner, M. Merz, S. Schuppler, P. Nagel, A. B. Muñoz-García, M. Pavone, H. A. Gasteiger, M. Piana, *J. Electrochem. Soc.* **2019**, *166*, F3032.
[68] T. Mittermeier, P. Madkikar, X. Wang, H. A. Gasteiger, M. Piana, *J. Electrochem. Soc.* **2016**, *163*, F1543.
[69] Y.-S. Li, D. Menga, H. A. Gasteiger, B. Suthar, *J. Electrochem. Soc.* **2023**, *170*, 094503.
[70] A. Siebel, Y. Gorlin, J. Durst, O. Proux, F. Hasché, M. Tromp, H. A. Gasteiger, *ACS Catal.* **2016**, *6*, 7326.
[71] C. Simon, F. Hasché, H. A. Gasteiger, *J. Electrochem. Soc.* **2017**, *164*, F591.
[72] B. Ravel, M. Newville, *J. Synchrotron Radiat.* **2005**, *12*, 537.

Manuscript received: March 14, 2024
Revised manuscript received: June 20, 2024
Version of record online: August 26, 2024